TECHNISCHE
UNIVERSITÄT
WIEN

Master Thesis

Direct Numerical Simulation of Stably Stratified Turbulence under Oberbeck-Boussinesq Hypotheses at High Reynolds and Richardson Numbers

carried out for the purpose of obtaining the degree of

Master of Science (MSc)

submitted at Technische Universität Wien

Faculty of Mechanical and Industrial Engineering

by

Pejman Hadi Sichani, BSc

Mat.Nr.: 1227115

under the supervision of

Univ.Prof. Dipl.-Ing. Dr.-Ing.Alfredo Soldati

Institute of Fluid Mechanics and Heat Transfer

Affidavit

I declare in lieu of oath, that I wrote this thesis and performed the associated research myself, using literature cited in this volume. If text passages from sources are used literally, they are marked as such.

I confirm that this work is original and has not been submitted elsewhere for any examination, nor is it currently under consideration for a thesis elsewhere.

Vienna, October, 2018

_____

Signature

Abstract

In this thesis, we focus on stably stratified turbulent channel flow at high shear Reynolds number Re_τ. We performed an extensive campaign of pseudo-spectral direct numerical simulations (DNS) of the governing equations (written under OB approximation) in the shear Richardson number space $Ri_\tau = Gr/Re_\tau^2$, where Gr is the Grashof number. Specifically, we fix the Reynolds number $Re_\tau = 1000$ and we change Gr so to cover a broad range of Ri_τ values. Our results of stratified turbulence indicate that the average and turbulent fields undergo significant variations compared to the case of forced convection, in which temperature is a passive scalar ($Ri_\tau = 0$). In particular, we observe that turbulence is actively sustained only near the boundaries, whereas intermittent turbulence, also flavored by the presence of non-turbulent wavy structures (Internal Gravity Waves, IGW) is observed at the core of the channel. Naturally, the interaction between turbulence and stratification alters also the overall transfer rates of momentum an heat. We believe that the present results may give an important contribution to future turbulence modeling in this field.

Kurzfassung

Im Rahmen dieser Diplomarbeit werden stabile turbulente Schichtenströmungen in einem Kanal bei einer, mit der Schubspannungsgeschwindigkeit u_τ gebildeten, Reynolds-Zahl $Re_\tau = 1000$. Umfangreiche direkte numerische Simulationen der Grundgleichungen (unter Verwendung der Oberbeck-Boussinesq Approximation) wurden mit Hilfe einer Pseudospectralmethode für unterschiedliche Richardson-Zahlen $Ri_\tau = Gr/Re_\tau^2$, mit der Grashof-Zahl Gr, durchgeführt. Um einen großen Bereich an Richardson-Zahlen abzudecken, wird bei konstanter Reynolds-Zahl die Grashof-Zahl variiert. Sowohl für das gemittelte, als auch für das turbulente Strömungsfeld zeigen die Ergebnisse der geschichteten Turbulenz stark unterschiedliches Verhalten im Vergleich zum Fall der erzwungenen Konvektion, bei der sich die Temperatur passiv verhält. Im speziellen beobachten wir Aufrechterhaltung der Turbulenz nur in Wandnähe, wobei intermittierende Turbulenz, beeinflusst von der Anwesenheit nicht turbulenter welliger Strukturen (interne Schwerewellen), auch in Kanalmitte auftritt. Natürlicherweise verursacht die Wechselwirkung zwischen Turbulenz und Schichtung eine Veränderung von globalem Impuls- und Wärmeaustausch. Unserer Ansicht nach liefern die Ergebnisse dieser Arbeit einen wichtigen Beitrag für zukünftige Turbulenzmodelle im Bereich der Schichtenströmungen.

Acknowledgments

Contents

List of Figures

List of tables

Nomenclature

Abbreviations

2D	Two Dimensional
3D	Three Dimensional
DNS	Direct Numerical Solution
FD	Finite difference
FE	Finite element
FV	Finite volume
IGW	Internal Gravity Wave
IMEX	Implicit/Explicit
MPI	Message Passing Interface
NOB	Non-Oberbeck-Boussinesq
OB	Oberbeck-Bussinesq
PS	Pseudospectral
RMS	Root Mean Square

Greek Symbols

β	Thermal expansion coefficient
ΔT	Temperature difference
δ	Non-dimensional parameter
$\delta_{1,i}$	Mean pressure gradient
$\delta_{i,3}$	Kronecker delta
ϵ	Turbulent kinetic energy dissipation rate
$\epsilon_1, ... \epsilon_{12}$	Non-dimensional parameters
η	Kolmogorov length scale
η_B	Batchelor scale

γ	Fluid property coefficient
Γ_{ij}	Rate of strain tensor
κ_T	Turbulent eddy diffusivity
λ	Thermal conductivity
μ	Dynamic Viscosity
ν_T	Turbulent eddy viscosity
ω	Vorticity vector
Φ	Rate of dissipation of mechanical energy due to viscosity
ρ	Density
τ_w	Wall shear stress

Latin Symbols

a, b, c, d, e, f, m, n	Fluid property coefficients
c	Speed of sound
c_p	Specific heat coefficient
g	Gravitational acceleration
Gr	Grashof number
h	Half-channel height
k	Wave number
Ma	Mach number
N	Brunt–Väisälä frequency
Nu	Nusselt number
Nu_c	Centerline Nusselt number
P	Pressure
p	Fluctuating kinematic pressure
P_0	Reference pressure
Pr	Prandtl number
Pr_T	Turbulent Prandtl number
q_w	Mean heat flux
Re_τ	Shear Reynolds number
Re_b	Bulk Reynolds number

Ri_τ	Shear Richardson number
Ri_b	Bulk Richardson number
Ri_f	Flux Richardson number
Ri_g	Gradient Richardson number
S	Mean shear rate
T	temperature
t	Time
T'	Temperature fluctuations
T_0	Reference temperature
T_C	Cold wall temperature
T_H	Hot wall temperature
T_W	Wall temperature
u'	Streamwise velocity fluctuations
u_b	Bulk velocity
u_i	i^{th} component of the velocity vector
u_τ	Friction velocity
v'	Spanweise velocity fluctuations
w'	Wall-normal velocity fluctuations
x	Streamwise direction
y	Spanwise direction
z	Wall-normal direction
z^-	Dimensionless wall-normal coordinate

1 Introduction

Turbulent stratified flows are of great interests due to their importance in industrial, environmental and geophysical applications. Industrial applications in which turbulent stratified flows commonly occur, include cooling in nuclear reactors [15], fluid motion in heat transfer equipments [52], or fuel injection and combustion in gasoline engines [20]. Natural processes include the dynamics of the nocturnal atmospheric boundary layer [37], mixing in rivers and continental shelf seas [70], or the transport of organic species in the ocean [71].

The problem of stratified turbulence is fairly complex. In addition to the complexity of turbulence itself, we have to also take the presence of buoyancy forces that do depend on local density gradients into account. For a comprehensive determination of a turbulent stratified flow, it is required to specify a number of parameters. These parameters include the flow forcing and boundary conditions, the mean temperature gradient, and the fluid properties like density, viscosity, thermal conductivity, thermal expansion coefficient and specific heat. Other factors that may be important include concentration and salinity gradients, rotational and multiphase flow effects, phase change, flow compressibility and specific dependence of the fluid properties on the local temperature and pressure field. Critical applications often involve many of these complicating factors at once [77]. For example, fuel injection and combustion in gasoline engines involves strong localized variations of fluid properties, flow compressibility, multiphase flow effects and phase change [20]. Stratified turbulence can be unbounded and homogeneous, as in the stratosphere or in the deep ocean [32], [34], [55]. However, stratified turbulence can be also unbounded and sheared, as for instance when the wind blows in the atmosphere or when deep currents stir the ocean [11], [60], [61], and finally stratified turbulence can be bounded and sheared, as in the terrestrial and oceanic boundary layers [37], [45], [71] or in industrial applications [16]. When stratified turbulence is homogeneous, turbulence is not sustained by any applied shear and decays following an evolution in which buoyancy forces influence the largest flow scales first, and the smaller scales later, until the final turbulence collapse is reached [61]. When stratified turbulence is forced by an applied uniform shear, its dynamics is controlled by the gradient Richardson number $Ri_g = N^2/S^2$, with S the value of the mean shear and N the Brunt-Väisälä frequency. Numerical and experimental results [27], [58] indicate that if $Ri_g \simeq 0.25$ the turbulence neither grows nor decay. At lower values of Ri_g turbulence grows, whereas at higher ones it decays. Finally, when stratified turbulence is forced by an applied shear and at the same time influenced by the presence of a boundary, its evolution is not only controlled by the mean strength

of shear and stratification, but also by their distributions as a function of the distance from the boundary [3]. In this work, we will have the case of wall-bounded stratified turbulence. Wall-bounded stably stratified flows can be divided into two main categories, which are commonly referred to as the weakly/moderately and the strongly stratified case (or alternatively, weakly stable and very stable regimes [36]). In the weakly/moderately stratified case, turbulence is actively sustained near the boundary, whereas intermittent turbulence, also flavored by the presence of non-turbulent wavy structures (Internal Gravity Waves, IGW [63]), is observed at larger distances. In this case, an equilibrium regime is established between the production of turbulence by the mean shear and the suppression of turbulence by the stable stratification so that the Monin-Obhukov self similarity theory [40], [47] can be used. In the strongly stratified case, a global turbulent state cannot be sustained. As a result the flow becomes intermittent, with regions characterized by a complete turbulence suppressions, followed by regions in which turbulence is reactivated. In this work, we will have the case of weakly/moderately stratified turbulence.

In this work, wall-bounded stably stratified turbulence is described performing Direct Numerical Simulations (DNS) of the continuity, Navier-Stokes and energy equations under Oberbeck-Bussinesq (OB) approximation. The outline of this thesis is as following. Chapter 2 documents the physical modeling and mathematical formulation of the problem. The numerical approach and discretization of the equations are described in chapter 3. In chapter 4, plan of the numerical experiments, velocity and temperature statistics, qualitative behavior of the flow field and also the characterization of the flow state as a function of stratification is presented. The main conclusions of the work are summarized in chapter 5.

2 Physical Modeling of the Problem

In this section we present the physical and mathematical models used to described wall-bounded stably stratified turbulent flows. Specifically, in section 2.1 we introduce the general compressible form of the governing equations (Non-Oberbeck-Boussinesq, NOB). In section 2.2 will will introduce the Oberbeck-Boussinesq (OB) approximation and provide a discussion on the ranges of validity of the OB approximation.

2.1 General Form of the Governing Equations

The most general starting point for the analysis of stably-stratified turbulence is represented by the complete system of continuity, momentum and energy equations for a Newtonian fluid of variable properties and second viscosity equal to zero [6]. This set of equations in dimensional form (denoted by the superscript *) is:

$$\frac{D\rho^*}{Dt^*} + \rho^* \frac{\partial u_i^*}{\partial x_i^*} = 0 \ , \tag{2.1}$$

$$\rho^* \frac{Du_i^*}{Dt^*} = -\frac{\partial P^*}{\partial x_i^*} - \rho^* g^* \delta_{3,i}^* + \mu^* \frac{\partial \Gamma_{ij}^*}{\partial x_j^*} + \Gamma_{ij}^* \frac{\partial \mu^*}{\partial x_j^*} \ , \tag{2.2}$$

$$\rho^* c_p^* \frac{DT^*}{Dt^*} = \lambda^* \frac{\partial^2 T^*}{\partial x_j^{*2}} + \frac{\partial \lambda^*}{\partial x_j^*}\frac{\partial T^*}{\partial x_j^*} + \beta^* T^* \frac{DP^*}{Dt^*} + \mu^* \Phi^* \ , \tag{2.3}$$

where u_i^* is the ith component of the velocity vector, P^* is pressure, T^* is temperature and g^* is the gravitational acceleration. Note that

$$\Gamma_{ij}^* = \frac{\partial u_i^*}{\partial x_j^*} + \frac{\partial u_j^*}{\partial x_i^*} - \frac{2}{3}\frac{\partial u_k^*}{\partial x_k}\delta_{ij}^*, \quad \Phi = \frac{1}{2}\Gamma_{ij}^* \left(\frac{\partial u_i^*}{\partial x_j^*} + \frac{\partial u_j^*}{\partial x_i^*} \right) \tag{2.4}$$

are the rate of strain tensor (Γ_{ij}^*) and the rate of dissipation of mechanical energy due to viscosity (Φ^*). The termophysical fluid properties are density ρ^*, viscosity μ^*, specific heat c_p^*, thermal conductivity λ^* and thermal expansion coefficient $\beta^* = -1/\rho^* \left(\partial \rho^* / \partial T^* \right)_p$. To fully specify the problem, suitable laws for the determination of the fluid properties

as a function of temperature and pressure must be prescribed. These can be given in the general form:

$$\rho^* = \rho^*(T^*, P^*) \tag{2.5}$$

$$c_p^* = c_p^*(T^*, P^*) \tag{2.6}$$

$$\mu^* = \mu^*(T^*, P^*) \tag{2.7}$$

$$\beta^* = \beta^*(T^*, P^*) \tag{2.8}$$

$$\lambda^* = \lambda^*(T^*, P^*) \tag{2.9}$$

In most cases, such laws are inferred from available analytical expressions and correlations derived from thermodynamics and/or experimental measurements [4], [42], [59], [74], [75]. Eqs. 2.1-2.3, complemented with explicit laws to particularize Eqs. 2.5-2.9, constitute the general form of the governing equations. In connection with the following section, and precisely to stress the difference with the commonly adopted Oberbeck-Boussinesq (OB) approximation, this form is usually called Non-Oberbeck-Boussinesq (NOB).

2.2 Oberbeck-Boussinesq (OB) approximation

The Oberbeck-Boussinesq (OB) approximation [8], [46] is based on the assumption that fluid density variations are small enough to be negligible in the continuity equation and play a role only in the gravitational term of the momentum equation (i.e. where ρ^* is multiplied by the acceleration due to gravity g^*). The reason why is it possible to assume a constant ρ^* but in the gravitational term, is that the product $\rho^* g^*$ can produce large effects even when relative density fluctuations with respect to the reference density ρ_0^* are very small (i.e. $(\rho^* - \rho_0^*)/\rho_0^* \ll 1$), since acceleration due to gravity is in general much larger than any other local value of the fluid acceleration (i. e. $|g^*| \gg |Du_i^*/Dt^*|$). Further, in the OB approximation all thermophysical fluid properties are strictly constant and uniform.

2.2.1 Governing Equations

The governing equations can be conveniently written in dimensionless form. Without loss of generality, we refer to the case of a density stratified Poiseuille flow in a closed channel, in which the stable stratification is maintained by keeping a positive density difference $\Delta\rho^* = \rho_b^* - \rho_t^*$ between the bottom (ρ_b^*) and the top (ρ_t^*) walls. The OB form of the governing balance equations in dimensional form and in tensor notation (repeated index implies summation) reads as:

$$\frac{\partial u_i^*}{\partial x_i^*} = 0 \ , \tag{2.10}$$

$$\rho^* \frac{\partial u_i}{\partial t^*} = -\rho^* u_j^* \frac{\partial u_i^*}{\partial x_j^*} + \mu^* \frac{\partial^2 u_i^*}{\partial x_j^{*2}} - \frac{\partial p^*}{\partial x_i^*} + \left(\rho^* - \rho_{ref}^* \right) g^* + \delta_{1,i}^*, \tag{2.11}$$

$$\rho^* c_p^* \frac{\partial T^*}{\partial t^*} + \rho^* c_p^* u_j^* \frac{\partial T^*}{\partial x_j^*} = \lambda^* \frac{\partial^2 T^*}{\partial x_j^{*2}}, \tag{2.12}$$

where p^* is the fluctuating kinematic pressure and $\delta_{1,i}^*$ is the mean pressure gradient that drives the flow. Variables are made dimensionless as follows:

$$\rho = \frac{\rho^*}{\rho_0^*}; \qquad \mu = \frac{\mu^*}{\mu_0^*}; \qquad \lambda = \frac{\lambda^*}{\lambda_0^*}; \qquad c_p = \frac{c_p^*}{c_{p,0}^*};$$

$$\mathbf{x} = \frac{\mathbf{x}^*}{h^*}; \qquad \mathbf{u} = \frac{\mathbf{u}^*}{u_\tau^*}; \qquad t = \frac{t^* u_\tau}{h^*}; \qquad p = \frac{p^*}{\rho_0^* u_\tau^{*2}}; \qquad T = \frac{T^* - T_0^*}{\Delta T^*/2};$$

where h^* is the half-channel height and $\Delta T^* = T_H^* - T_C^*$ (T_H^* is the temperature of the hot wall while T_C^* is the temperature of the cold wall). The reference velocity for adimensionalization is the friction velocity $u_\tau^* = \sqrt{\frac{\tau_w^*}{\rho_0^*}}$, where τ_w^* is the shear stress at the wall, whereas the reference temperature is the centerline temperature $T_0^* = \left(T_H^* + T_C^* \right)/2$. Note that subscript *0* is used to represent thermophysical fluid properties at the reference temperature.

With the assumption of uniform thermophysical properties, the governing balance equations (Eq. 2.10-2.12) in dimensionless form read as:

$$\frac{\partial u_i}{\partial x_i} = 0 \ , \tag{2.13}$$

$$\frac{\partial u_i}{\partial t} = S_i + \frac{1}{Re_\tau} \left(\frac{\partial^2 u_i}{\partial x_j^2} \right) - \frac{\partial p}{\partial x_i} \ , \tag{2.14}$$

$$\frac{\partial T}{\partial t} = S_T + \frac{1}{Re_\tau Pr} \left(\frac{\partial^2 T}{\partial x_j^2} \right). \tag{2.15}$$

The *S*-terms contain the non-linear convective terms, the dimensionless mean pressure gradient and the buoyancy term:

$$S_i = -u_j \frac{\partial u_i}{\partial x_j} + \delta_{i,1} - \delta_{i,3} \frac{1}{16} \frac{Gr}{Re_\tau^2} T, \tag{2.16}$$

$$S_T = -u_j \frac{\partial T}{\partial x_j} \ . \tag{2.17}$$

In the above equations, $\delta_{i,3}$ is the Kronecker delta (used to account for the buoyancy term in the wall-normal direction only), whereas

$$Re_\tau = \frac{\rho_0^* u_\tau^* h^*}{\mu_0^*}, \qquad Pr = \frac{\mu_0^* c_{p,0}^*}{\lambda_0^*}, \qquad Gr = \frac{g^* \beta_0^* \Delta T^* (2h^*)^3}{(\nu_0^*)^2},$$

are respectively the Reynolds number, the Prandtl number and the Grashof number, defined in terms of the termophysical properties at the rference temperature T_0^*. In the definition of the Grashof number, $\beta_0^* = -\frac{1}{\rho^*} \left(\frac{\partial \rho^*}{\partial T^*} \right)_p$ and $\nu_0^* = \frac{\mu_0^*}{\rho_0^*}$ are the thermal expansion coefficient and the kinematic viscosity at the reference temperature. As apparent, Eqs. 2.13-2.17 include buoyancy effects. However, the same equations can be used to analyze neutrally-buoyant flows, simply assuming a vanishing Grashof number ($Gr = 0$). It is worth mentioning that the term $\left(\frac{Gr}{Re_\tau^2} \right)$ is equal to Richardson number (Ri) and therefor in a neutrally-buoyant case Ri is equal to zero. Alternative definitions of the Richardson number are used in literature to describe and parameterize the dynamics of stratified turbulence. The different definitions of the Richardson numbers are based on different definitions of the reference velocity scale used to write equations in dimensionless form. Therefore, we have the centerline Richardson number (which takes the centerline velocity u_c as reference), the bulk Richardson number Ri_b (which takes the bulk velocity u_b as reference) and the gradient Richardson number $Ri_g = N^2/S^2$ (which takes the Brunt–Väisälä frequency N and the mean shear rate S as reference parameters). Although Ri_τ is customarily used for the characterization of the flow regimes in numerical simulations of wall-bounded stratified flows [3], [21], [22], its use in experiments is much more limited. Reasons are related to the difficulty in the determination of the shear velocity u_τ (that in turn requires the determination of the wall shear stress). Therefore, in experiments the bulk Richardson number Ri_b is usually preferred, since the bulk velocity is an easier quantity to access.

2.2.2 Range of validity of the approximate equations

A number of important aspects of the flow physics in the field of stably stratified flows [7], [23], [68] was elucidated by employing the OB approximation (Eqs. 2.13-2.15). It should be remarked here, however, that it represents a good approximation of the exact equations (Eqs. 2.1-2.3) within certain ranges of variation of the main parameters only [25], [38], [43], [44], [62], and its applicability beyond these ranges is not physically justified. To understand it, we estimate the accuracy error introduced by the assumption of constant density in the continuity equation by computing the ratio between the material derivative of density $\rho^{-1} D\rho/Dt$ and the divergence of the velocity field $\partial u_j/\partial x_j$ [31], [67]. Upon introduction of appropriate length (l_0), velocity (u_0) and temperature (ΔT) scales, we get

$$\frac{\rho^{-1} D\rho/Dt}{\partial u_j/\partial x_j} = \frac{\beta DT/Dt}{\partial u_j/\partial x_j} \simeq \frac{\beta \Delta T (u_0/l_0)}{u_0/l_0} = \beta \Delta T. \tag{2.18}$$

To derive Eq. 2.18, u_0 is considered small compared to the speed of sound c (i.e. the Mach number $Ma = u_0/c < 0.3$) and pressure changes in the fluid are considered slow compared to acoustic pressure waves. Therefore, for the OB approximation to be valid, $\beta \Delta T \ll 1$. However, this represents only a rough estimate. Precise boundaries for the validity of the OB approximation were obtained by Gray and Giorgini [25] starting from the full non-linear equations in compressible form and writing all the fluid properties as a linear Taylor expansion of temperature and pressure, i.e.:

$$\rho = \rho_0 \left[1 - \beta_0 \left(T - T_0\right) + \gamma_0 \left(P - P_0\right)\right],$$
$$c_p = c_{p0} \left[1 - a_0 \left(T - T_0\right) + b_0 \left(P - P_0\right)\right],$$
$$\mu = \mu_0 \left[1 - c_0 \left(T - T_0\right) + d_0 \left(P - P_0\right)\right],$$
$$\beta = \beta_0 \left[1 - e_0 \left(T - T_0\right) + f_0 \left(P - P_0\right)\right],$$
$$\lambda = \lambda_0 \left[1 - m_0 \left(T - T_0\right) + n_0 \left(P - P_0\right)\right].$$

where

$$a = \frac{1}{c_p}\frac{\partial c_p}{\partial T}, \quad b = \frac{1}{c_p}\frac{\partial c_p}{\partial P}, \quad c = \frac{1}{\mu}\frac{\partial \mu}{\partial T}, \quad d = \frac{1}{\mu}\frac{\partial \mu}{\partial P},$$

$$e = \frac{1}{\beta}\frac{\partial \beta}{\partial T}, \quad f = \frac{1}{\beta}\frac{\partial \beta}{\partial P}, \quad m = \frac{1}{\lambda}\frac{\partial \lambda}{\partial T}, \quad n = \frac{1}{\lambda}\frac{\partial \lambda}{\partial P},$$

$$\beta = -\frac{1}{\rho}\frac{\partial \rho}{\partial T}, \quad \gamma = \frac{1}{\rho}\frac{\partial \rho}{\partial P},$$

are the fluid property coefficients and the subscript 0 denotes the reference state (T_0, P_0).

After retaining only the leading order terms of the resulting equations, Gray and Giorgini [25] were able to derive a set of constraints for the OB approximation to be valid. These constraints were written in the following form:

$$\epsilon_1 = \beta_0 \Delta T \leq \delta, \quad \epsilon_2 = \gamma_0 \rho_0 g h \leq \delta,$$

$$\epsilon_3 = c_0 \Delta T \leq \delta, \quad \epsilon_4 = d_0 \rho_0 g h \leq \delta,$$

$$\epsilon_5 = a_0 \rho_0 g h \leq \delta, \quad \epsilon_6 = b_0 \rho_0 g h \leq \delta,$$

$$\epsilon_7 = m_0 \Delta T \leq \delta, \quad \epsilon_8 = n_0 \rho_0 g h \leq \delta,$$

$$\epsilon_9 = e_0 \Delta T \le \delta, \qquad \epsilon_{10} = f_0 \rho_0 gh \le \delta,$$

$$\epsilon_{11} = \beta_0 gh/cp_0 \le \delta,$$

$$\epsilon_{12} = \epsilon_{11} T_0/\Delta T \le \delta,$$

where $\delta = 0.1$ is a small enough number (i.e. giving a maximum error of 10% in the estimate of the fluid property). That is to say, when $\delta \le 0.1$, the value of each fluid property can be safely approximated by its reference value. A further restrictive condition, i.e. $\epsilon_{12} < 0.02$, for the work done by pressure forces and the heat generated by viscous losses to be negligible, has been recently proposed by Pons and Quéré [53]. Altogether, these constraints set the boundaries for an explicit evaluation of the validity ranges of the OB approximation. These are plotted in figure 2.1 for the case of air (Fig. 2.1a) and water (Fig. 2.1b) at reference temperature $T_0 = 15^o C$ and pressure $P_0 = 10^5 Pa$. The two main parameters are the temperature difference ΔT and the characteristic size of the problem h. The values of the thermophysical properties at the reference conditions are evaluated as in [25].
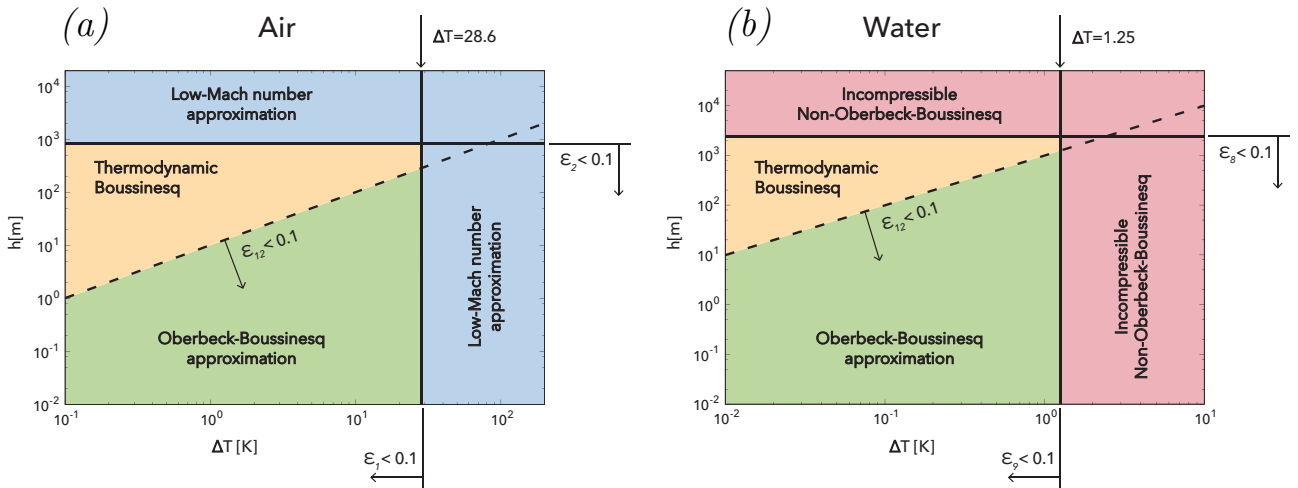
Figure 2.1: A parameter space $(\Delta T, h)$ of wall-bounded stably stratified turbulence with the different numerical approach that can be used for its description. Panel a): air; panel b): water (Reproduced with permission from Zonta and Soldati [77]. Copyright 2018 by ASME)

In figure 2.1, the solid lines indicate approximately the point at which the basic Oberbeck-Boussinesq model begins to fail, and more complex Non-Oberbeck-Boussinesq models (both incompressible NOB or Low-Mach) must be used. The dashed line indicates the point at which the thermodynamic Boussinesq model should be used. Specific indication of the parameter (ϵ) that describes each threshold line is also explicitly given. The color of each region indicates a specific numerical approach according to the following color-

code: Oberbeck-Boussinesq (green), Low-Mach number Approach (cyan), Incompressible NOB (pink), thermodynamic Boussinesq (yellow). Some examples of the most suitable approaches to be used for flows of interest in environmental and industrial applications are provided in the following. In the nocturnal boundary layer, for example, $h \simeq 10^2/10^3 \ m$ and $\Delta T \simeq 5 \ ^oC$. In this case, the Thermodynamic Boussinesq model would be appropriate. However, if $h > 10^3 \ m$, a Low-Mach number approach would be recommended. In the deep ocean, $h \simeq 10^3 \ m$ and $\Delta T \simeq 2 \ ^oC$, whereas in the upper ocean, $h \simeq 10^2 \ m$ and $\Delta T \simeq 10 \ ^oC$ [51]. In both cases, an Incompressible NOB approach is required. In industrial heat transfer processes, typical sizes are $h \simeq 1 \ m$, whereas ΔT are usually larger than in environmental applications. For air, temperature gradients can easily be $\Delta T = 10/100 \ ^oC$ while for water ΔT can achieve few tens, in particular for high heat flux cooling technologies [1]. In these latter cases, a Low Mach number approach (air) and an Incompressible NOB approach (water) is recommended.

For air, the most restrictive conditions are ϵ_1 (variation of ρ with T), ϵ_2 (variation of ρ with P) and ϵ_{12} (pressure work term). For water, the most restrictive conditions are ϵ_9 (variation of β with T), ϵ_8 (variation of λ with P) and ϵ_{12} (pressure work term). Sometimes, when liquids are used as working fluids at a reference temperature different from the commonly adopted $T_0 = 15^oC$, ϵ_2 (variation of μ with temperature) can become as important as ϵ_9 (see for instance Zonta *et* al. [74], [75]) in determining the proper thresholds for the validity of the OB approximation.

The widely used OB approximation is physically sound in the green area of Fig. 2.1 only. The extended Boussinesq model (sometimes called thermodynamic Boussinesq model, see [53]) accounting for the pressure-work term in the energy equation has a validity that includes also the yellow region in Fig. 2.1. Outside these ranges, NOB approaches must be used. While the low-Mach number approximation (also known as anelastic approximation [5], [33], [48], cyan regions in Fig. 2.1) are required for air flows (since the most restrictive condition is the dependence of ρ on T and P), alternative solutions accounting for the temperature or pressure variation of μ, β or λ [64], [75], [76] are adequate for water (and other liquid) flows in many situations far from critical points (pink regions in Fig. 2.1). The case of liquid flows close to critical conditions must be analyzed with a low-Mach number approximation as well [4], [42], [59].

3 Methodology

3.1 An introduction to pseudospectral method

The partial differential equations that arise in applications can only rarely be solved in closed form. Even when they can be, the solutions are often impractical to work with and to visualize. Numerical techniques, on the other hand, can be applied successfully to virtually all well posed partial differential equations. Broadly applicable techniques include finite element (FE), finite volume (FV), finite difference (FD), and, more recently, spectral methods. The complexity of the domain and the required levels of accuracy are often the key factors in selecting among these approaches. Finite-element methods are particularly well suited to problems in very complex geometries (e.g. 3D engineering structures), whereas spectral methods can offer superior accuracies (and cost efficiencies) mainly in simple geometries such as boxes and spheres (which can, however, be combined into more complex shapes). FD methods perform well over a broad range of accuracy requirements and (moderately complex) domains. Both FE and FV methods are closely related to FD methods. FE methods can frequently be seen as a very convenient way to generate and administer complex FD schemes and to obtain results with relatively sharp error estimates. The connection between spectral methods, in particular the so-called pseudospectral (PS) methods and FD methods is closer still.

Finite difference methods approximate derivatives of a function by local arguments (such as $du/dx \sim [u(x+h) - u(x-h)]/2h$, where h is a small grid spacing; these methods are typically designed to be exact for polynomials of low order). This approach is very reasonable: because the derivative is a local property of a function (which need not be smooth), it seems unnecessary (and is certainly costly) to invoke many function values far away from the point of interest. In contrast, spectral methods are global. A common way to introduce them starts by approximating the function we want to differentiate as a sum of very smooth basis functions:

$$u(x) \approx \sum_{k=0}^{N} a_k \phi_k(x), \tag{3.1}$$

where the $\phi_k(x)$ are for example Chebyshev polynomials or trigonometric functions. We then differentiate these functions exactly. In the context of solving time-dependent PDEs, this approach has notable strengths.

- For analytic functions, errors typically decay (as N increases) at exponential rather than at (much slower) polynomial rates.

- The method is virtually free of both dissipative and dispersive errors.

  - In the context of solving high-Reynolds number fluid flows, the low physical dissipation will not be overwhelmed by large numerical dissipation. For convection-type problems, sharp gradients in a solution will not turn into wavetrains because of dispersive errors (making different frequency components propagate at different speeds).

- The approach is surprisingly powerful for many cases in which both solutions and variable coefficients are nonsmooth or even discontinuous.

- Especially in several space dimensions, the relatively coarse grids that suffice for most accuracy requirements allow very time- and memory efficient calculations.

However, the following factors can cause difficulties or inefficiencies when using spectral methods:

- certain boundary conditions;

- irregular domains;

- strong shocks;

- variable resolution requirements in different parts of a large domain;

In some applications- where these disadvantages are not present or can somehow be overcome - FE, FV, or FD methods do not even come close in efficiency. However, in most areas of application the situation is not so clear-cut. At present, spectral methods are highly successful in several areas: turbulence modeling, weather prediction, nonlinear waves, seismic modeling and etc [18].

3.2 Numerical approach

In this section, the numerical approach developed for the solution of Eqs. (2.13)-(2.15) is discussed. To lighten the form of the equations, a simplified notation will be use in the following section (Sec. 3.3): x_1, x_2 and x_3 represent the streamwise, the spanwise and the wall normal-directions, whereas u_1, u_2 and u_3 are the corresponding velocity components.

3.3 Solution Procedure

The present scheme solves for the balance equations of motion (Eqs. 2.13-2.15) through the elimination of pressure. The pressure field can be removed upon taking the curl of Eq. (2.14), to give:

$$\frac{\partial \omega_k}{\partial t} = \epsilon_{ijk}\frac{\partial S_j}{\partial x_i} + \frac{1}{Re}\nabla^2\omega_k, \tag{3.2}$$

where $\omega_k = \epsilon_{ijk}\frac{\partial u_j}{\partial x_i}$ is the $k-th$ component of the vorticity vector. Note that the $S-$terms in (3.2) have already been introduced in section 2.2.1. Taking twice the curl of Eq. (2.14) and using Eq. (2.13) together with the vectorial identity $\nabla \times (\nabla \times \mathbf{v}) = \nabla(\nabla \cdot \mathbf{v}) - \nabla^2\mathbf{v}$, a 4th-order equation in u_i can be obtained:

$$\frac{\partial(\nabla^2 u_i)}{\partial t} = \nabla^2 S_i - \frac{\partial}{\partial x_i}\left(\frac{\partial S_j}{\partial x_j}\right) + \frac{1}{Re}\nabla^4 u_i. \tag{3.3}$$

Eqs. (3.2)-(3.3) can be written with respect to the normal components, *i.e.* for ω_3 and u_3:

$$\frac{\partial \omega_3}{\partial t} = \frac{\partial S_2}{\partial x_1} - \frac{\partial S_1}{\partial x_2} + \frac{1}{Re}\nabla^2\omega_3. \tag{3.4}$$

$$\frac{\partial(\nabla^2 u_3)}{\partial t} = \nabla^2 S_3 - \frac{\partial}{\partial x_3}\left(\frac{\partial S_j}{\partial x_j}\right) + \frac{1}{Re}\nabla^4 u_3. \tag{3.5}$$

These two equations are numerically solved for ω_3 and u_3. With ω_3 and u_3 known, u_1 and u_2 can be obtained by solving the following equations simultaneously:

$$\frac{\partial u_1}{\partial x_1} + \frac{\partial u_2}{\partial x_2} = -\frac{\partial u_3}{\partial x_3}, \tag{3.6}$$

$$\frac{\partial u_2}{\partial x_1} - \frac{\partial u_1}{\partial x_2} = \omega_3. \tag{3.7}$$

Eqs. (3.6) and (3.7) derive, respectively, from continuity and from the definition of vorticity. Although not needed for time advancement of the solutions, pressure can be obtained by solving a Poisson-type equation after all velocity components have been found:

$$\nabla^2 p = \frac{\partial S_j}{\partial x_j}. \tag{3.8}$$

Once the velocity field is known, the temperature field can be obtained from the solution of the energy balance equation:

$$\frac{\partial T}{\partial t} = S_T + \frac{1}{Re_\tau Pr}\left(\frac{\partial^2 T}{\partial x_j{}^2}\right). \tag{3.9}$$

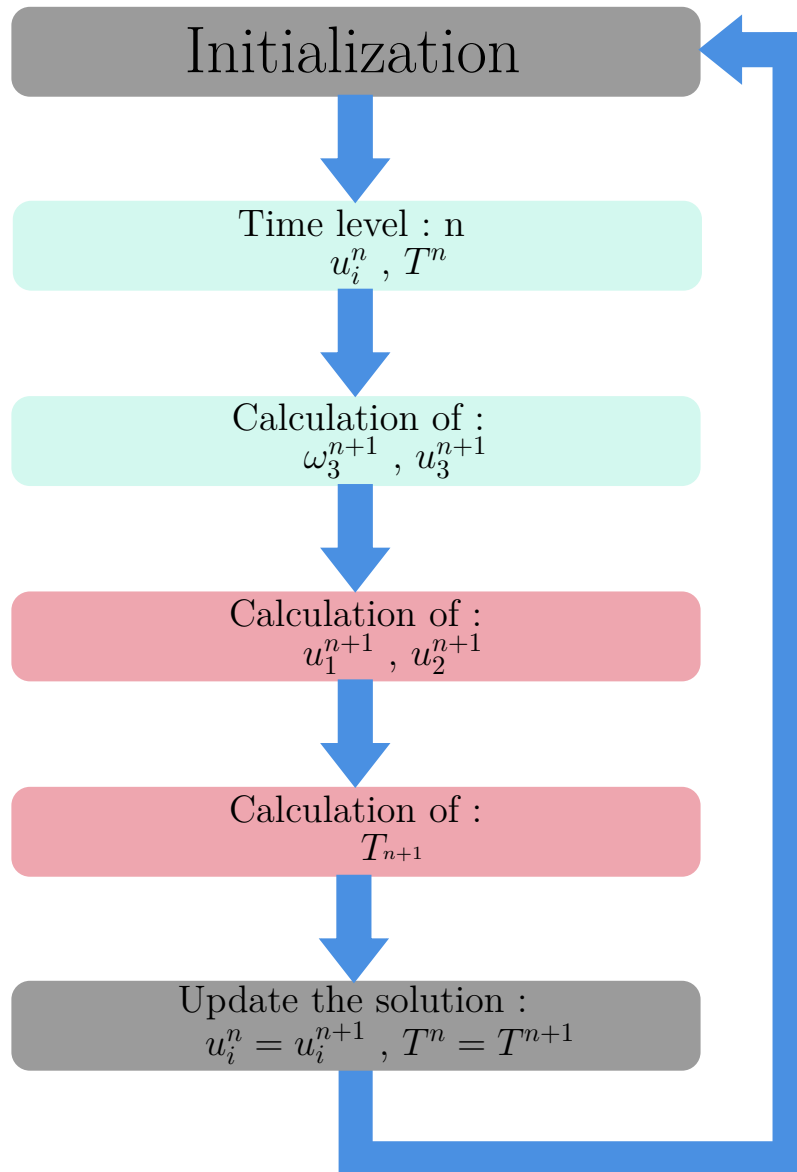A schematic representation of the algorithm is shown in Fig. 3.1.

Figure 3.1: Solver scheme

3.4 Spectral Representation of Solutions

To represent the solution in space, finite Fourier expansion in the homogeneous (x_1 and x_2) directions is used:

$$f(x_1, x_2, x_3) = \sum_{|n_1|}^{\frac{N_1}{2}} \sum_{|n_2|}^{\frac{N_2}{2}} \hat{f}(k_1, k_2, x_3) e^{i(k_1 x_1 + k_2 x_2)}, \tag{3.10}$$

where $\hat{f}$ represents the Fourier coefficients of a general dependent function, $i = \sqrt{-1}$, N_1 and N_2 are the number of Fourier modes retained in the series, and the summation indices n_1 and n_2 are chosen so that $-\frac{N_1}{2} + 1 \leq n_1 \leq \frac{N_1}{2}$ and $-\frac{N_2}{2} + 1 \leq n_2 \leq \frac{N_2}{2}$. The wavenumbers k_1 and k_2 are given by:

$$k_1 = \frac{2\pi n_1}{L_1} \tag{3.11}$$

$$k_2 = \frac{2\pi n_2}{L_2}, \tag{3.12}$$

with L_1 and L_2 being the periodicity lengths in the streamwise and spanwise directions. Because of the orthogonality of the Fourier functions, the Fourier transform $\hat{f}$ can be obtained as:

$$\hat{f}(k_1, k_2, x_3) = \frac{1}{N_1 N_2} \sum_{|n_1|}^{\frac{N_1}{2}} \sum_{|n_2|}^{\frac{N_2}{2}} f(x_1, x_2, x_3) e^{-i(k_1 x_1 + k_2 x_2)}, \tag{3.13}$$

where x_1 and x_2 are chosen to be the transform locations

$$x_1 = \frac{n_1}{N_1} L_1 \tag{3.14}$$

$$x_2 = \frac{n_2}{N_2} L_2. \tag{3.15}$$

In the cross-stream (wall-normal) direction x_3, Chebyshev polynomials are used to represent the solution,

$$\hat{f}(k_1, k_2, x_3) = \sum_{n_3=0}^{N_3'} a(k_1, k_2, n_3) T_n(x_3), \tag{3.16}$$

where the prime denotes that the first term is halved. The Chebyshev polynomial of order n_3 in x_3 is defined as

$$T_{n_3}(x_3) = \cos(n_3 \arccos(x_3)), \tag{3.17}$$

with $-1 \le x_3 \le 1$. Orthogonality also exist for Chebyshev polynomials, which leads to the following inverse transformation:

$$\hat{a}(k_1, k_2, n_3) = \frac{2}{N_3} \sum_{n_3=0}^{N_3'} \hat{a}(k_1, k_2, x_3) T_{n_3}(x_3). \tag{3.18}$$

In physical space the collocation points along the cross-stream direction are related to Chebyshev indexes in the following way:

$$x_3 = \cos\left(\frac{n_3 \pi}{N_3}\right), \tag{3.19}$$

The advantage of using Chebyshev polynomials to represent the solution in the cross-stream direction is that such a representation gives very good resolution in the regions close to the boundaries, because the collocation points bunch up there [1]. In Fig. 3.2, a representation of the first six polynomials is given. For in-depth discussion on Chebyshev polynomials and their applications in numerical analysis, see Fox and Parker [19]. There-
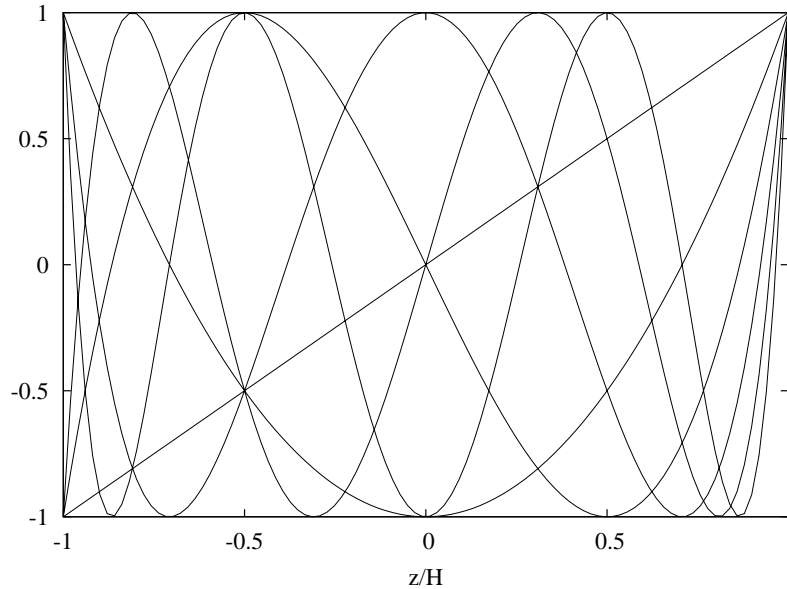

Figure 3.2: The Chebishev polynomials $T_r(x_3)$ (with $r = 0, ..6$) in computational space for $-1 \le x_3 \le 1$.

fore, the spectral representation (in all three directions) of a generic dependent variable takes the final form

$$f(x_1, x_2, x_3) = \sum_{|n_1|}^{\frac{N_1}{2}} \sum_{|n_2|}^{\frac{N_2}{2}} \sum_{n_3=0}^{N_3'} \hat{a}(k_1, k_2, n_3) e^{i(k_1 x_1 + k_2 x_2)} T_{n_3}(x_3), \tag{3.20}$$

---

[1]In wall bounded flows, resolution close to the wall is very important, since large gradients of the solutions occur there

3.5 Discretization of the equations

3.5.1 Momentum equations

With the spectral representation given by Eq. (3.10), Eq. (3.5) can be written as:

$$
\frac{\partial}{\partial t}\left(\frac{\partial^2}{\partial x_3^2} - k^2\right)\hat{u}_3 = \left(\frac{\partial^2}{\partial x_3^2} - k^2\right)\hat{S}_3
$$

$$
- \frac{\partial}{\partial x_3}\left(ik_1\hat{S}_1 + ik_2\hat{S}_2 + \frac{\partial}{\partial x_3}\hat{S}_3\right) \tag{3.21}
$$

$$
+ \frac{1}{Re}\left(\frac{\partial^2}{\partial x_3^2} - k^2\right)\left(\frac{\partial^2}{\partial x_3^2} - k^2\right)\hat{u}_3,
$$

where $k^2 = k_1^2 + k_2^2$. Time advancement of Eq. (3.21) is done using a two-level explicit Adams-Bashfort scheme for the convective terms and an implicit Crank-Nicholson method for the diffusion terms. The time-differenced form of Eq. (3.21), based on the above schemes, is

$$
\left(\frac{\partial^2}{\partial x_3^2} - k^2\right)\frac{(\hat{u}_3^{n+1} - \hat{u}_3^n)}{\Delta t} = \frac{3}{2}\left(\frac{\partial^2}{\partial x_3^2} - k^2\right)\hat{S}_3^n - \frac{1}{2}\left(\frac{\partial^2}{\partial x_3^2} - k^2\right)\hat{S}_3^{n-1}
$$

$$
- \frac{\partial}{\partial x_3}\,ik_1(\frac{3}{2}\hat{S}_1^n - \frac{1}{2}\hat{S}_1^{n-1})
$$

$$
- \frac{\partial}{\partial x_3}\,ik_2(\frac{3}{2}\hat{S}_2^n - \frac{1}{2}\hat{S}_2^{n-1}) \tag{3.22}
$$

$$
- \frac{\partial^2}{\partial x_3^2}(\frac{3}{2}\hat{S}_3^n - \frac{1}{2}\hat{S}_3^{n-1})
$$

$$
+ \frac{1}{Re}\left(\frac{\partial^2}{\partial x_3^2} - k^2\right)\left(\frac{\partial^2}{\partial x_3^2} - k^2\right)\frac{(\hat{u}_3^{n+1} + \hat{u}_3^n)}{2},
$$

where superscripts $n-1$, n and $n+1$ indicate three successive time levels. By defining $\gamma = \frac{\Delta t}{2\,Re}$ we can rearrange Eq. (3.22):

$$\left[1 - \gamma\left(\frac{\partial^2}{\partial x_3^2} - k^2\right)\right]\left(\frac{\partial^2}{\partial x_3^2} - k^2\right)\hat{u}_3^{n+1} =$$
$$- k^2(\frac{3}{2}\hat{S}_3^n - \frac{1}{2}\hat{S}_3^{n-1})\Delta t$$
$$- \frac{\partial}{\partial x_3}\,ik_1(\frac{3}{2}\hat{S}_1^n - \frac{1}{2}\hat{S}_1^{n-1})\Delta t \qquad (3.23)$$
$$- \frac{\partial}{\partial x_3}\,ik_2(\frac{3}{2}\hat{S}_2^n - \frac{1}{2}\hat{S}_2^{n-1})\Delta t$$
$$+ (\gamma\frac{\partial^2}{\partial x_3^2} + (1 - \gamma k^2))\left(\frac{\partial^2}{\partial x_3^2} - k^2\right)\hat{u}_3^n.$$

Introducing $\beta^2 = \frac{1+\gamma k^2}{\gamma}$ and recalling that $\frac{\partial \hat{u}_3}{\partial x_3} = -ik_1\hat{u}_1 - ik_2\hat{u}_2$ from continuity, we can manipulate the last term on the RHS of Eq. (3.23):

$$- \gamma\left(\frac{\partial^2}{\partial x_3^2} - \beta^2\right)\left(\frac{\partial^2}{\partial x_3^2} - k^2\right)\hat{u}_3^{n+1} =$$
$$- k^2(\frac{3}{2}\hat{S}_3^n - \frac{1}{2}\hat{S}_3^{n-1})\Delta t - k^2(\gamma\frac{\partial^2}{\partial x_3^2} + (1 - \gamma k^2))\hat{u}_3^n$$
$$- \frac{\partial}{\partial x_3}\,ik_1(\frac{3}{2}\hat{S}_1^n - \frac{1}{2}\hat{S}_1^{n-1})\Delta t - \frac{\partial}{\partial x_3}\,ik_1(\gamma\frac{\partial^2}{\partial x_3^2} + (1 - \gamma k^2))\hat{u}_1^n \qquad (3.24)$$
$$- \frac{\partial}{\partial x_3}\,ik_2(\frac{3}{2}\hat{S}_2^n - \frac{1}{2}\hat{S}_2^{n-1})\Delta t - \frac{\partial}{\partial x_3}\,ik_2(\gamma\frac{\partial^2}{\partial x_3^2} + (1 - \gamma k^2))\hat{u}_2^n$$
$$.$$

By introducing the historical terms:

$$\hat{H}_1^n = (\frac{3}{2}\hat{S}_1^n - \frac{1}{2}\hat{S}_1^{n-1})\Delta t + (\gamma\frac{\partial^2}{\partial x_3^2} + (1 - \gamma k^2))\hat{u}_1^n,$$
$$\hat{H}_2^n = (\frac{3}{2}\hat{S}_2^n - \frac{1}{2}\hat{S}_2^{n-1})\Delta t + (\gamma\frac{\partial^2}{\partial x_3^2} + (1 - \gamma k^2))\hat{u}_2^n, \qquad (3.25)$$
$$\hat{H}_3^n = (\frac{3}{2}\hat{S}_3^n - \frac{1}{2}\hat{S}_3^{n-1})\Delta t + (\gamma\frac{\partial^2}{\partial x_3^2} + (1 - \gamma k^2))\hat{u}_3^n,$$

Eq. (3.24) becomes:

$$\left(\frac{\partial^2}{\partial x_3^2} - \beta^2\right)\left(\frac{\partial^2}{\partial x_3^2} - k^2\right)\hat{u}_3^{n+1} = \frac{1}{\gamma}(k^2\hat{H}_3^n + \frac{\partial}{\partial x_3}(ik_1\hat{H}_1^n + ik_2\hat{H}_2^n)). \qquad (3.26)$$

If we put $\hat{H}^n = k^2 \hat{H}_3^n + \frac{\partial}{\partial x_3}(ik_1 \hat{H}_1^n + ik_2 \hat{H}_2^n)$ we come to the final form of the equation:

$$\left(\frac{\partial^2}{\partial x_3^2} - \beta^2\right)\left(\frac{\partial^2}{\partial x_3^2} - k^2\right)\hat{u}_3^{n+1} = \frac{\hat{H}^n}{\gamma}. \tag{3.27}$$

Defining $\hat{\phi} = \left(\frac{\partial^2}{\partial x_3^2} - k^2\right)\hat{u}_3^{n+1}$ the above fourth-order equation becomes a system of two second-order equations:

$$\left(\frac{\partial^2}{\partial x_3^2} - \beta^2\right)\hat{\phi} = \frac{\hat{H}^n}{\gamma}, \tag{3.28}$$

$$\left(\frac{\partial^2}{\partial x_3^2} - k^2\right)\hat{u}_3^{n+1} = \hat{\phi}. \tag{3.29}$$

These equations are solved with the following four boundary conditions:

$$\begin{aligned}
\hat{u}_3^{n+1}(\pm 1) &= 0 \qquad (a) \\
\frac{\partial \hat{u}_3^{n+1}}{\partial x_3}(\pm 1) &= 0 \qquad (b).
\end{aligned} \tag{3.30}$$

The lack of real boundary conditions for $\hat{\phi}$ can be circumvented by decomposing it into three parts:

$$\hat{\phi} = \hat{\phi}_1 + \hat{A}\phi_2 + \hat{B}\phi_3, \tag{3.31}$$

where constants $\hat{A}$ and $\hat{B}$ are to be determined. These three individual components of $\hat{\phi}$ satisfy:

$$\begin{aligned}
\left(\frac{\partial^2}{\partial x_3^2} - \beta^2\right)\hat{\phi}_1 &= \frac{\hat{H}^n}{\gamma}, & \hat{\phi}_1(1) &= 0, & \hat{\phi}_1(-1) &= 0; \\
\left(\frac{\partial^2}{\partial x_3^2} - \beta^2\right)\phi_2 &= 0, & \phi_2(1) &= 0, & \phi_2(-1) &= 1; \\
\left(\frac{\partial^2}{\partial x_3^2} - \beta^2\right)\phi_3 &= 0, & \phi_3(1) &= 1, & \phi_3(-1) &= 0.
\end{aligned} \tag{3.32}$$

Likewise $\hat{u}_3^{n+1}$ can be splitted into:

$$\hat{u}_3 = \hat{u}_{3,1} + \hat{A}u_{3,2} + \hat{B}u_{3,3}. \tag{3.33}$$

Once the solution of Eqs. (3.32) has been carried out, we can solve:

$$\left(\frac{\partial^2}{\partial x_3^2} - \beta^2\right)\hat{u}_{3,1} = \hat{\phi}_1, \qquad \hat{u}_{3,1}(1) = 0, \qquad \hat{u}_{3,1}(-1) = 0$$

$$\left(\frac{\partial^2}{\partial x_3^2} - \beta^2\right)u_{3,2} = \phi_2, \qquad u_{3,2}(1) = 0, \qquad u_{3,2}(-1) = 0 \qquad (3.34)$$

$$\left(\frac{\partial^2}{\partial x_3^2} - \beta^2\right)u_{3,3} = \phi_3, \qquad u_{3,3}(1) = 1, \qquad u_{3,3}(-1) = 0.$$

Finally the unknown constants $\hat{A}$ and $\hat{B}$ are determined applying the boundary conditions of Eq. (3.30b) to $\hat{u}_3^{n+1}$ written in terms of its components:

$$\frac{\partial \hat{u}_{3,1}}{\partial x_3}(1) + \hat{A}\frac{\partial u_{3,2}}{\partial x_3}(1) + \hat{B}\frac{\partial u_{3,3}}{\partial x_3}(1) = 0,$$
$$\frac{\partial \hat{u}_{3,1}}{\partial x_3}(-1) + \hat{A}\frac{\partial u_{3,2}}{\partial x_3}(-1) + \hat{B}\frac{\partial u_{3,3}}{\partial x_3}(-1) = 0. \qquad (3.35)$$

With $\hat{A}$ and $\hat{B}$ determined, $\hat{u}_3^{n+1}$ is fully known. The above systems of equations are solved using a Chebyshev method so the solutions $\hat{u}_3^{n+1}$ will be represented by Chebyshev coefficients in the wall normal direction x_3. Therefore, the solution $\hat{u}_3^{n+1}$ will be be function of k_1, k_2 and n_3:

$$\hat{u}_3^{n+1} = \hat{u}_3^{n+1}(k_1, k_2, n_3), \qquad (3.36)$$

where $0 < n_3 < N_3$, N_3 being the number of coefficients and collocation points in the wall normal direction. Recalling Eq. (3.10), the solution in space will read as:

$$u_3^{n+1}(x_1, x_2, x_3) = \sum_{|n_1|}^{\frac{N_1}{2}}\sum_{|n_2|}^{\frac{N_2}{2}}\sum_{n_3=0}^{N_3'} \hat{u}_3^{n+1}(k_1, k_2, n_3)e^{i(k_1 x_1 + k_2 x_2)}T_{n_3}(x_3), \qquad (3.37)$$

The other two velocity components will be determined through the normal vorticity component $\hat{\omega}_3$. Following a discretization procedure similar to that of Eq. (3.5), we can write:

$$\left(\frac{\partial^2}{\partial x_3^2} - \beta^2\right)\hat{\omega}_3^{n+1} = -\frac{(ik_1\hat{H}_2^n - ik_2\hat{H}_1^n)}{\gamma}, \qquad (3.38)$$

with boundary conditions:

$$\hat{\omega}_3^{n+1} = ik_1\hat{u}_2 - ik_2\hat{u}_1 = 0 \qquad x_3 = \pm 1. \qquad (3.39)$$

Once vorticity is known, $\hat{u}_1^{n+1}$ and $\hat{u}_2^{n+1}$ can be determined from solving:

$$-ik_2\hat{u}_1^{n+1} + ik_1\hat{u}_2^{n+1} = \hat{\omega}_3^{n+1}, \qquad (3.40)$$

$$ik_1\hat{u}_1^{n+1} + ik_2\hat{u}_2^{n+1} = -\frac{\partial \hat{u}_3^{n+1}}{\partial x_3}, \qquad (3.41)$$

that come from the definition of $\hat{\omega}_3$ and from continuity equation, respectively. Pressure can be calculated by the transformed Poisson equation Eq. (3.8):

$$\left(\frac{\partial^2}{\partial x_3^2} - \beta^2\right)\hat{p}^{n+1} = ik_1\hat{S}_1^{n+1} + ik_2\hat{S}_2^{n+1} + \frac{\partial \hat{S}_3^{n+1}}{\partial x_3}. \tag{3.42}$$

Boundary conditions for $\hat{p}^{n+1}$ can be obtained by the transformed form of Eq. (2.11) in the x_3 direction applied at $x_3 = \pm 1$.

The above scheme is used to evaluate the solutions in the Fourier-Chebyshev space for $k^2 \neq 0$. The case $k^2 = 0$ corresponds to the solution averaged over an $x_1 - x_2$ plane. In this case the solution procedure is simpler: upon time discretization the x_1 and x_2 components of Eq. (2.14) in the Fourier-Chebyshev space after time discretization give:

$$\left(\frac{\partial^2}{\partial x_3^2} - \frac{1}{\gamma}\right)\hat{u}_1^{n+1} = -\frac{\hat{H}_1}{\gamma}, \tag{3.43}$$

$$\left(\frac{\partial^2}{\partial x_3^2} - \frac{1}{\gamma}\right)\hat{u}_2^{n+1} = -\frac{\hat{H}_2}{\gamma}, \tag{3.44}$$

that can be solved by applying the following boundary conditions:

$$\hat{u}_1^{n+1} = \hat{u}_2^{n+1} = 0 \qquad x_3 \pm 1. \tag{3.45}$$

Using the continuity equation, Eq. (3.41), with $k_1 = k_2 = 0$ and the condition $\hat{u}_3^{n+1}(\pm 1) = 0$ one can show that $\hat{u}_3^{n+1} = 0$. To calculate $\hat{p}^{n+1}$ it is necessary to recall the transformed momentum equation, Eq. (2.14), in the x_3 direction for $k^2 = 0$ and $\hat{u}_3^{n+1} = 0$: we have $\hat{p}^{n+1} = -(\widehat{u_3^{n+1}u_3^{n+1}})$.

3.5.2 Energy equation

Once the velocity field is given, then the thermal field can be computed solving Eq. (2.15). The convective term S_T is advanced in the time integration by the second order explicit Adams-Bashfort scheme, while the implicit Crank-Nicolson method is used to advance the diffusion term. The time differenced energy equation (Eq. 2.12) is therefore given by:

$$\frac{\hat{T}_i^{n+1} - \hat{T}_i^n}{\Delta T} = \frac{3}{2}\hat{S}_T^n - \frac{1}{2}\hat{S}_T^{n-1} + \frac{1}{PrRe_\tau}\frac{\partial^2}{\partial x_j \partial x_j}\left(\frac{T_i^{n+1} + T_i^n}{2}\right) \tag{3.46}$$

All n and $n-1$ terms are grouped into the historical term

$$\hat{H}_T = \left[\gamma_T\frac{\partial^2}{\partial z^2} + \left(1 - \gamma_T k^2\right)\right]\hat{T}^n + \Delta T\left(\frac{3}{2}\hat{S}_T^n - \frac{1}{2}\hat{S}_T^{n-1}\right), \tag{3.47}$$

where $k^2 = k_1^2 + k_2^2$, $\gamma_T = \frac{\Delta t}{2Pr \cdot Re_\tau}$. Upon rearrangement the following differential equation for the temperature field can be obtained:

$$\left(\frac{\partial^2}{\partial z^2} - \frac{1 + \gamma_T^2}{\gamma_T} \right) \hat{T} = -\frac{\hat{H}_T}{\gamma_T}, \tag{3.48}$$

as an unknown for each Fourier wave number pair (k_1, k_2). Eq. (3.48) can be solved with a Chebishev-Tau method to obtain the new temperature field.

3.6 Direct numerical simulation (DNS)

Turbulence is characterized by a broad range of spatial scales. At one extreme of the scale domain we have the Kolmogorov length scale [54]

$$\eta = \left(\frac{\nu_0^3}{\epsilon} \right)^{1/4}, \tag{3.49}$$

which is the smallest flow scale that can be observed in a turbulent environment without being dissipated into heat by viscosity. Note that ϵ is the turbulent kinetic energy dissipation rate. Direct Numerical Simulation (DNS) discretize the governing equations on a spatio-temporal grid fine enough to resolve all the scales of the turbulent motion down to the Kolmogorov scale η for $Pr < 1$ or by the Batchelor scale $\eta_B = \eta/Pr$ for $Pr > 1$ [41], [54]. In unstratified wall-bounded turbulence, vertical scales are usually smaller (but of the same order of magnitude) than horizontal scales. In stratified wall-bounded turbulence, the scale separation becomes larger, with the vertical scales being usually orders of magnitude smaller than the horizontal scales. This poses further constraints on the computational cost of each simulation.

Since DNS computes turbulence without the aid of any model, it has the unique capability to capture all the flow details and to quantify all terms in the fundamental energy and momentum budgets, even those that cannot be experimentally measured. This is of specific importance for strongly stratified flows, where vigorous local turbulence events and sharp gradients of temperature and/or of material properties may lead to strong, spatially and temporally localized mixing and transport that may be remarkably different from the mean turbulence statistics. Many DNS studies of wall bounded stratified turbulence have been performed in closed or open plane channels and using different computational techniques. While simulations run in closed channels aim at mimicking internal flows of interest for industrial applications [21], [29], [73], [75], simulations in open channels and boundary layers [9], [10], [14], [17], [26], [35], [45], [70] are mostly motivated by environmental and geophysical applications (terrestrial and oceanic boundary layers). Despite some differences that may arise from the specific boundary conditions adopted,

stratification in open channels and boundary layers is similar to that observed in closed channels.

DNS of stably stratified channel turbulence was first performed by Iida *et* al. [29] for weakly/moderately stratified conditions in a closed channel at shear Reynolds number $Re_\tau = 150$, and by Nieuwstadt [45] for strongly stratified conditions in an open channel flow at shear Reynolds number $Re_\tau = 395$. Few years later, the DNS studies of Flores and Riley [17] and García-Villalba and del Álamo [21] have largely contributed to the physical comprehension of the dynamics of wall-bounded stratified turbulence. One of the crucial aspects raised by these DNS studies was the need of very large domains to properly characterize the turbulent structures present in stratified channels. This is of specific importance for strongly-stratified conditions, in which stratification effects fall well into the near-wall region inducing localized relaminarization patterns and a corresponding flow intermittency. The parameter range was further widened by subsequent works, increasing both the Reynolds and the Richardson numbers [9], [13], [70] so to explore weakly and strongly stratified conditions at values of Re_τ and Ri_τ progressively closer to those characterizing real applications. Recently, [26] has performed DNS of an open channel flow at the unprecedented values of the Reynolds number $Re_\tau = 10^3$ and Richardson number $Ri_\tau = 10^4$ (a combination leading to a bulk Reynolds number of the order of $Re = 10^5$), obtaining intriguing results on the phenomenon of global intermittency in the strongly stable regime.

In this thesis we performed DNS for a turbulent flow of air in a plane close channel with different constant wall temperatures, as sketched in figure 3.3. Setup parameters of our simulations are described in more detail in section 4.1. We run different simulations using a FORTRAN code which is parallelized with Message Passing Interface (MPI) and is highly scalable. The number of Fourier collocation points in streamwise and spanwise direction and also the number of Chebyshev polynomials in wall normal direction is chosen to fulfill the requirements imposed by the DNS for all different simulations. The time integration algorithm follows an implicit/explicit (IMEX) scheme. The nonlinear term is discretized in time using either an explicit Euler scheme (for the first time step only) either an Adams–Bashforth scheme (from the second time step on). For the implicit part the Crank–Nicolson algorithm is used.To decompose the domain we used a 2D domain decomposition which is shown in figure 3.4 (note that here N is the number of processors).
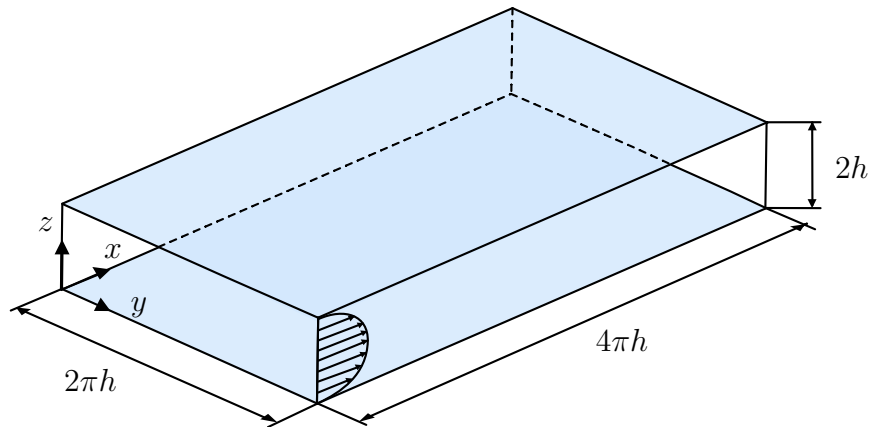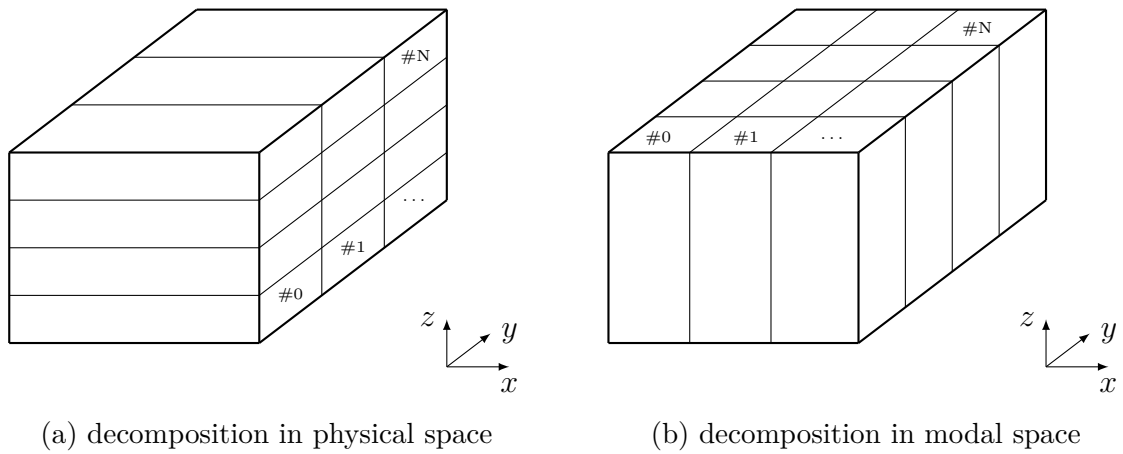
Figure 3.3: Sketch of the computational domain

(a) decomposition in physical space

(b) decomposition in modal space

Figure 3.4: 2D domain decomposition

4 Results

4.1 Plan of the numerical experiments

In this thesis, stably stratified turbulent flow between two walls is simulated directly. The fluid is driven by an imposed pressure gradient and the upper wall is kept at a constant temperature which is larger than the constant lower wall temperature. We performed DNS of thermally stratified flow for air and therefore Prandtl number is $Pr = 0.71$ for all cases. All simulations are at shear Reynolds number $Re_\tau = 1000$. The reference geometry consists of two infinite flat parallel walls. The $x-$, $y-$ and $z-$axis point in the streamwise, spanwise and wall-normal directions. The size of the channel is $4\pi h \times 2\pi h \times 2h$ in x, y and z, respectively (as presented in figure 3.3). Buoyancy acts along the wall-normal direction (z). Table 4.1 represents an overview of our simulations for different shear Richardson numbers Ri_τ.

Case	Ri_τ	Re_b	Nu_c	Size	Grid
$S0$	0	18850	29.8	$4\pi h \times 2\pi h \times 2h$	$1024 \times 1024 \times 513$
$S1$	6.25	19650	22	$4\pi h \times 2\pi h \times 2h$	$1024 \times 1024 \times 513$
$S2$	12.5	20170	18.4	$4\pi h \times 2\pi h \times 2h$	$1024 \times 1024 \times 513$
$S3$	25	20845	13.6	$4\pi h \times 2\pi h \times 2h$	$1024 \times 1024 \times 513$

Table 4.1: Overview of simulations at $Re_\tau = 1000$

In table 4.1 Re_b is the bulk Reynolds number and is defined as :

$$Re_b = \frac{u_b h}{\nu}$$

where u_b is the bulk velocity. The centreline Nusselt number Nu_c is also defined as :

$$Nu_c = \frac{q_w h}{\lambda(T_W - T_0)}$$

where $q_w = \lambda \partial \langle T \rangle / \partial z$ is the mean heat flux and T_W is the wall temperature. We recall here that T_0 is the reference temperature (centerline temperature). The time and space averaging are computed after reaching statistically the steady state turbulence over a sufficient long time window.

4.1.1 Velocity statistics

In figure 4.1 the mean streamwise velocity profiles, $\langle u \rangle$, are shown as a function of the dimensionless wall-normal coordinate $z^- = z/h$ for different Ri_τ numbers. Brackets represents averaging in time and in space over the homogeneous directions. Figure 4.1 clearly illustrates a flow acceleration for increasing stratification. The mean streamwise velocity profiles collapse nicely in the near-wall region, whereas they are shifted towards large values for increasing Ri_τ in the channel center. The increase of the centerline velocity indicates an increase of the mass flow rate (i.e an increase of bulck velocity u_b and bulk Reynolds number Re_b) and a coresponding decrease of both friction factor and Nusselt number. Note that, for all simulations, the driving pressure gradient is held constant.
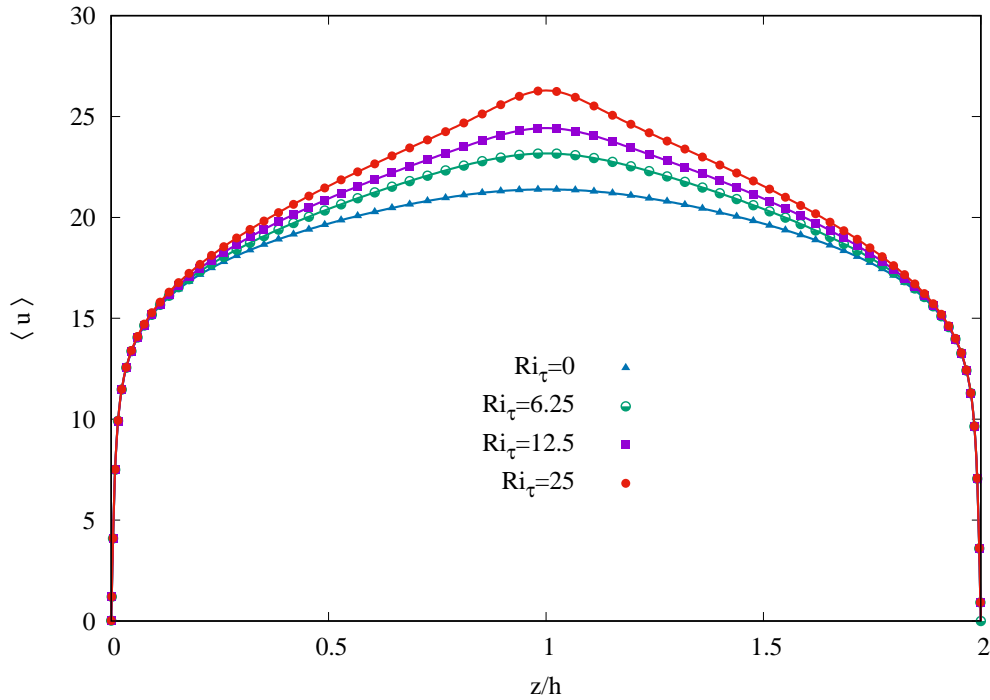
Figure 4.1: Mean streamwise velocity profile for different Ri_τ numbers

These observations clearly show that, stable stratification suppresses wall-normal momentum transport compared to the neutrally buoyant case, where temperature is a passive scalar. Suppression of wall-normal momentum transport is the consequence of the conversion of kinetic energy into potential energy occurring when a fluid particle is displaced in the wall-normal direction within the flow field. Since the driving pressure gradient is held constant among simulations, the viscous wall stress and, therefore, the slope of the mean velocity profile in the case of stable stratification should be invariant compared to those of the neutrally-buoyant case[75].

The root mean square (r.m.s.) of the fluid velocity fluctuations in all three directions (streamwise, spanwise an wall-normal) are shown in figures 4.2,4.3 and 4.4. In the near-wall region we observe a collapse for all three r.m.s of the velocity fluctuations. This suggests that near-wall turbulence is preserved for all different Richardson numbers. A very similar behavior was also observed in figure 4.1 for the mean streamwise velocity. As shown in figures 4.2 and 4.3, the r.m.s of streamwise and spanwise velocity decrease in the core region of the channel. Interestingly the r.m.s of the wall-normal velocity has a local maximum that can not be detected in the neutrally-buoyant flow. The local maximum of wall-normal velocity r.m.s associated distinctly with the effect of stratification in the core region of the channel.
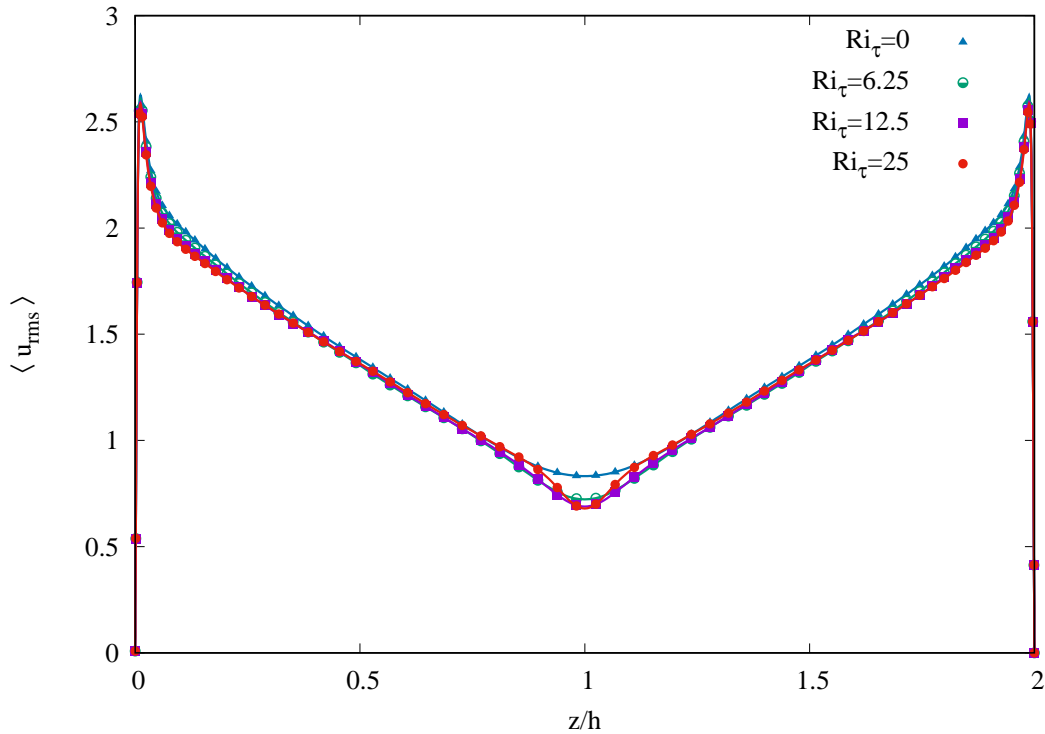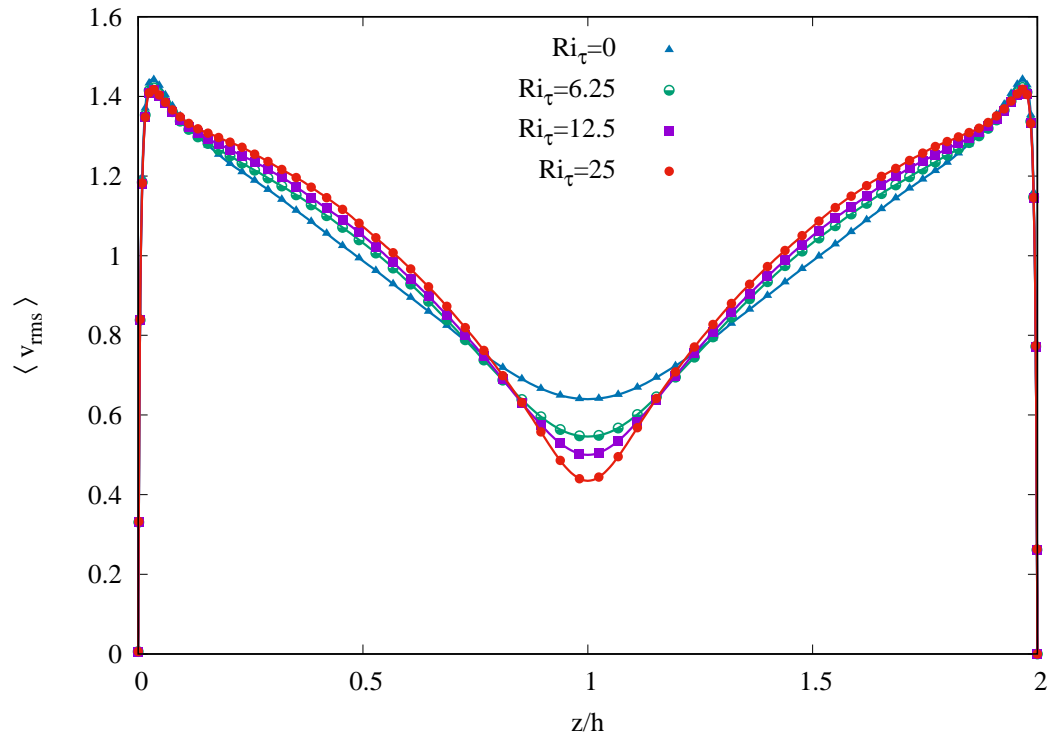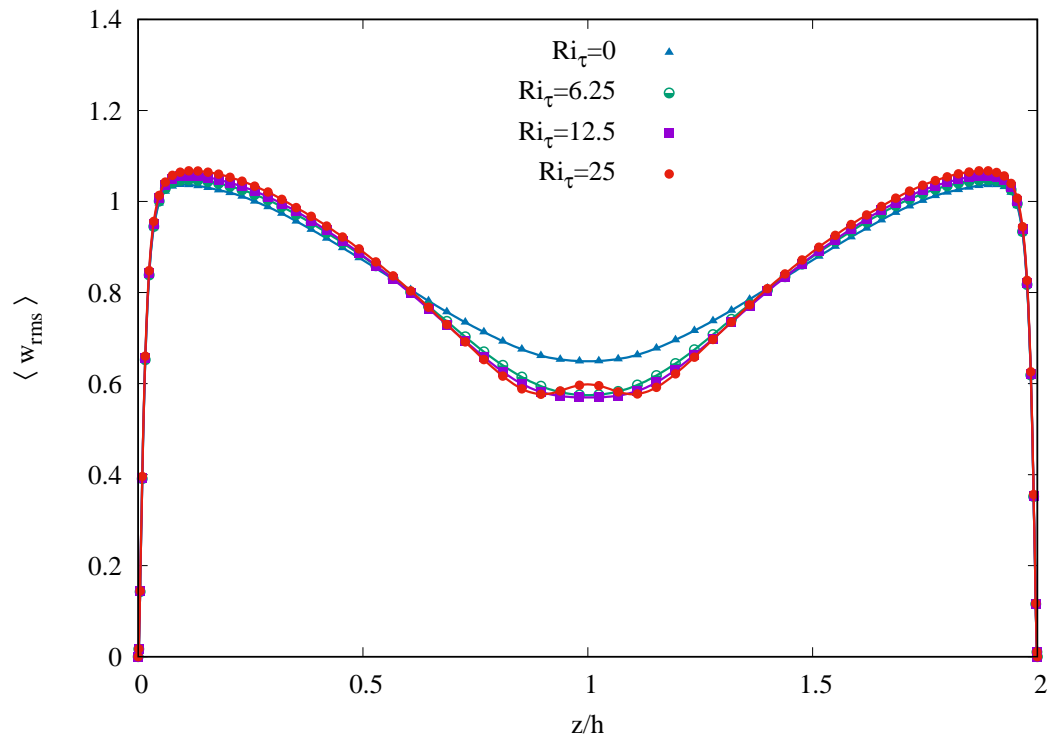

Figure 4.2: RMS streamwise velocity profile for different Ri_τ numbers

Figure 4.3: RMS spanwise velocity profile for different Ri_τ numbers

Figure 4.4: RMS wall-normal direction velocity profile for different Ri_τ numbers

4.1.2 Temperature statistics

In figure 4.5, the mean temperature profiles are shown for neutrally-buoyant and stratified cases. Stable stratification induces a sort of twofold effect on the temperature field compared to the neutrally-buoyant case. With increasing the level of stratification, the temperature gradient decreases at the wall (i.e. the Nusselt number) and simultaneously the temperature gradient increases at core region of the channel. In particular, the increased temperature gradient in the core of the channel indicates a tendency to form a kind of thick interface in this region. This interface, in which temperature changes more rapidly with depth than it does in the regions above or below, is usually called a *thermocline*[75]. Note that, due to symmetry condition , the shear becomes zero at the channel center where, as a consequence, buoyancy starts playing a dominant role.
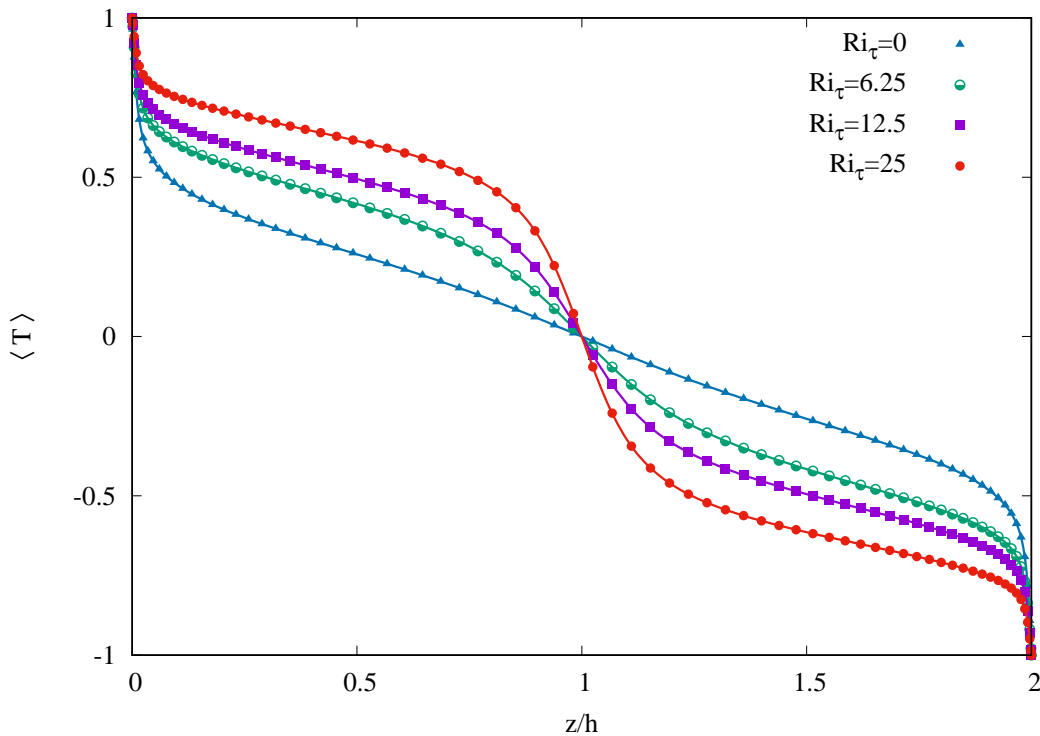
Figure 4.5: Mean temperature profile for different Ri_τ numbers

In figure 4.6, the root mean square of temperature fluctuations are shown for neutrally-buoyant and stratified cases. We observe that the peak value increases, with increasing the stratification level at core region of the channel.
The sequence of what we observed in figures 4.4 and 4.6 is a sort of consistent behavior between wall-normal velocity and temperature fluctuations at the core region of the channel. In particular, the internal gravity waves (IGW) involving w and T fluctuations only dominate the core region of stratified channel [21] and as a consequence, the

fluctuations in the core region of the channel may be associated with large-scale wavy motions (IGW) rather than with turbulence structures [75].
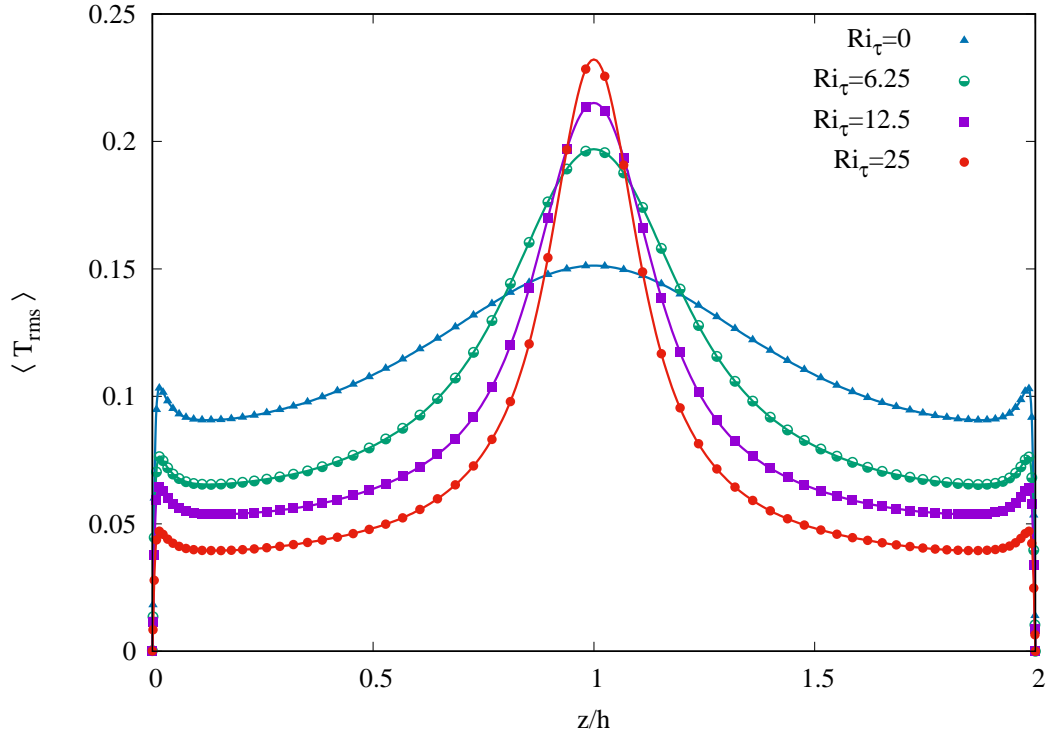

Figure 4.6: RMS temperature profile for different Ri_τ numbers

4.1.3 Velocity-temperature correlations

In figures 4.7 and 4.8 the correlations between velocity components and temperature fluctuations are shown. These correlations are usually called turbulent buoyancy fluxes. From figure 4.7, we can observe that the value of $\langle w'T' \rangle$ decreases significantly with increasing the level of stratification. We observed a remarkably different dynamics at the core region of the channel for stratified cases compared to the neutrally-buoyant case. The mean profiles and turbulent fluxes at the core region of the channel show a sort of more non-turbulent behavior in comparison to the near-wall region.The magnitude of temperature and wall-normal velocity fluctuations are noticeably large, as presented by figures 4.4 and 4.6. Although, the correlation between these two fluctuations, in particular $\langle w'T' \rangle$, is vary slight, as indicated by figure 4.7. This means, that such fluctuations are probably generated by internal gravity waves. We will deepen this discussion in section 4.3.
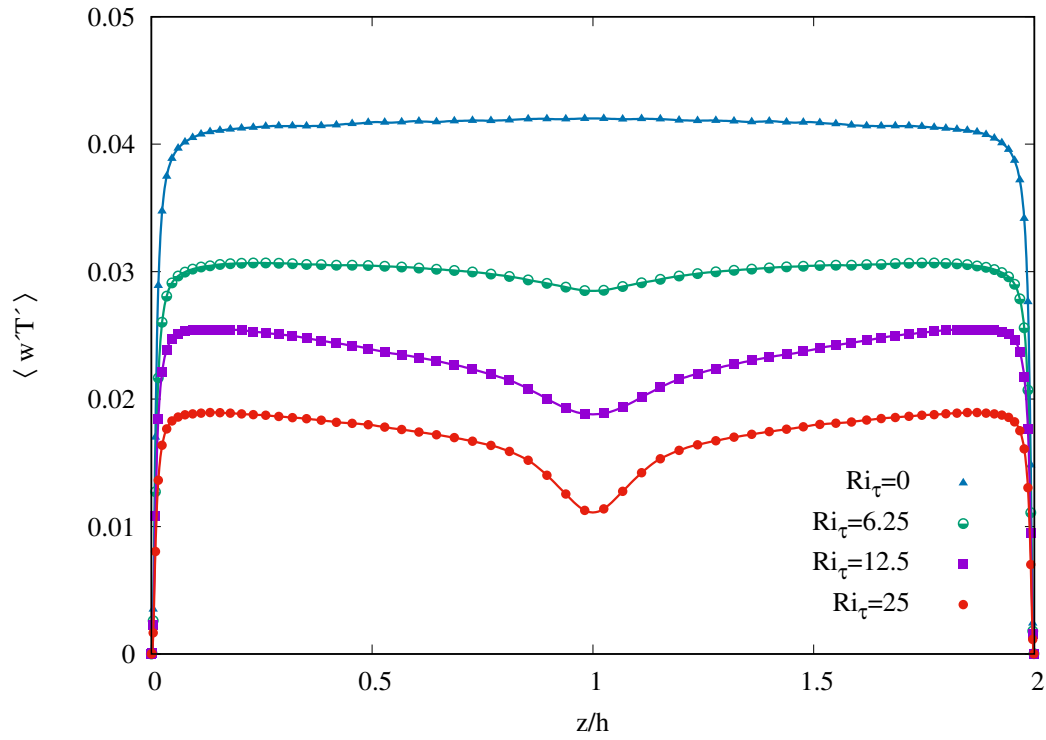
Figure 4.7: Turbulent buoyancy flux for different Ri_τ numbers
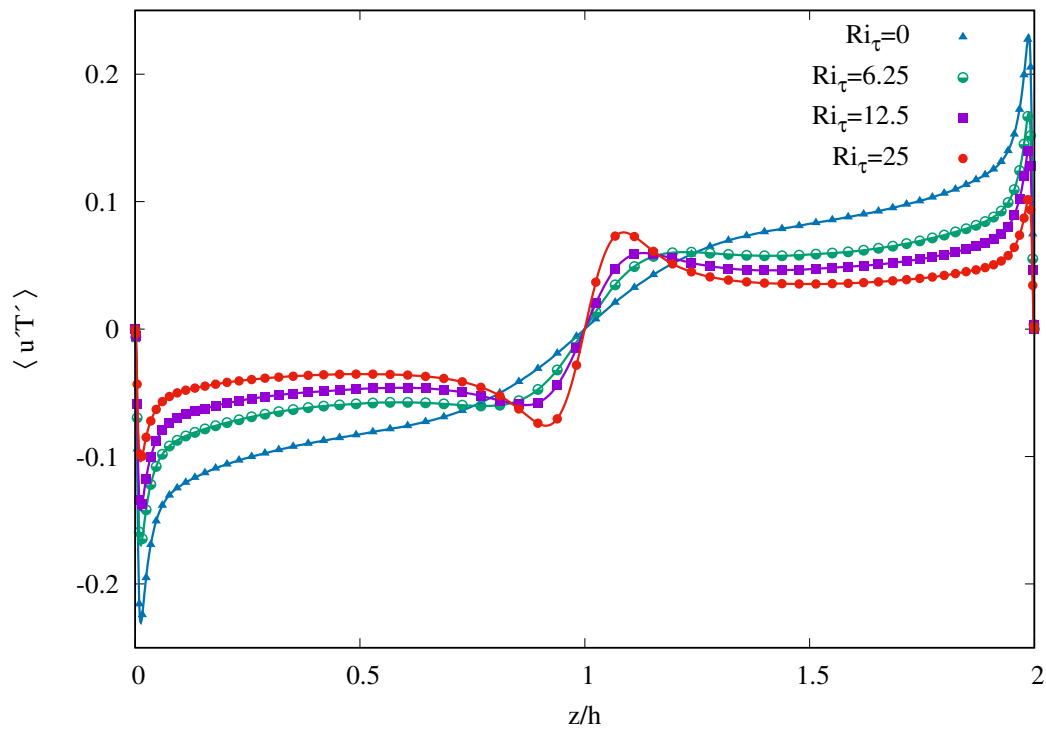
Figure 4.8: Temperature-velocity fluctuations correlation for different Ri_τ numbers

4.2 Characterization of the flow state as a function of the stratification

Stratified flows can support a variety of types of wave motions that cannot be observed in non-stratified flows. The reason is the tendency for wall-normal motion (the gravitational acceleration acting along the wall-normal direction) to be suppressed: a fluid particle that is displaced vertically by the wall-normal velocity fluctuations tends to be restored by gravity to its original position; it may overshoot inertially and oscillate about this position. The characteristic frequency of oscillation is called buoyancy frequency (or Brunt–Väisälä frequency) and can be computed as [75]:

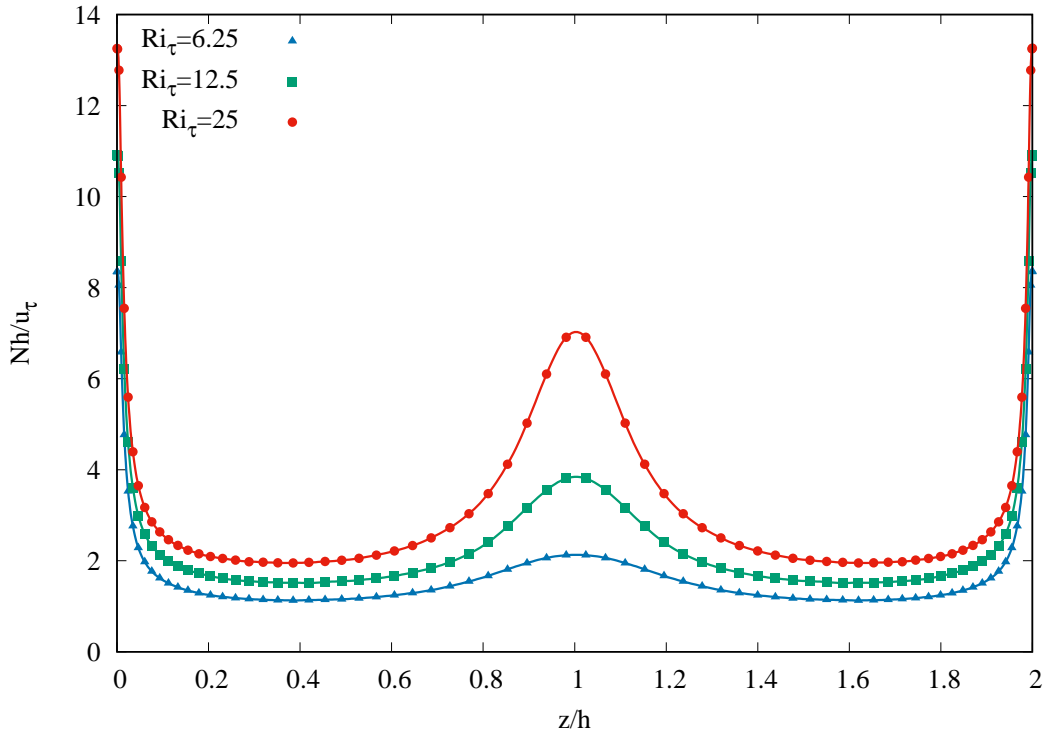$$N = \left(- g\beta \frac{\partial T}{\partial z} \right)^{\frac{1}{2}} \tag{4.1}$$

Figure 4.9: Buoyancy frequency, N as a function of vertical coordinate for different Ri_τ numbers

In figure 4.9, the dimensionless buoyancy frequency Nh/u_τ is shown as a function of the dimensionless wall-normal coordinate for different levels of stratification. We observe a sharp reduction of the buoyancy frequency in the near-wall region followed by an

approximately constant behavior in the buffer region of the channel. In the core region, the buoyancy frequency increases again. This behavior his is due to the fact that inside this region, internal gravity waves are dominating. In other words, the buoyancy effect modifies selectively the flow structure of the core region, but not of the near-wall region. With increasing the stratification, the peak value of the buoyancy frequency at the channel center grows, indicating that a stronger stratification influences more vigorously the structure of the core region. Such a behavior is directly linked to the significant changes of the temperature profile in the center of the channel (figure 4.5).

To characterize the flow state as a function of stratification, we follow archival literature ([68] [30]) in the field and we used the gradient Richardson number Ri_g:

$$Ri_g = \frac{N^2}{S^2} = \frac{-g\beta\frac{\partial T}{\partial z}}{\left(\frac{\partial <w>}{\partial z}\right)^2} \qquad (4.2)$$

where S is the shear rate. The gradient Richardson number is an important parameter, as shown in previos studies of homogeneous stratified turbulence [56] [28] that indicated $Ri_g \simeq 0.25$ as a critical value to understand the nature of the flow straucture. For $Ri_g \simeq 0.25$, the turbulence neither grows nor decay. At lower Richardson numbers turbulence grows, while at higher Richardson numbers turbulence decays. In particular in linear stability analysis [39], $Ri_g \geq 0.25$ is considered as a sufficient condition to obtains flow laminarization. Tis criterion has also been confirmed experimentally [57] [50]. In figure 4.10 the Ri_g is represented in logarithmic scale as a function of the dimensionless wall-normal coordinate for different Ri_τ numbers. In previous works Armenio and Sarkar [3], [66], García-Villalba and Álamo [21] and Zonta *et al* [75] observed a huge variation of Ri_g across the channel. Their results showed that Ri_g varied from very low values close to the wall to very large values close to the center of the channel. Figure 4.10 illustrates that our results are in a good agreement with their finding, in the channel center with the sharp increase of the slope of the profiles above $Ri_g \approx 0.25$. This huge variation of Ri_g along the wall-normal direction is due to the fact that in the core region $\partial\langle w\rangle/\partial z \to 0$ and therefor Ri_g is very large, while in the near-wall region $\partial\langle w\rangle/\partial z$ is large and Ri_g becomes small. In the center of the channel, due to the symmetry condition $\partial\langle w\rangle/\partial z = 0$ and Ri_g diverges. Another important observation from figure 4.10 is that the regions where Ri_g is bellow 0.25 are the turbulent regions, while the regions where Ri_g is above 0.25 are the regions where the turbulence is activity weakened and the internal gravity waves are dominant.
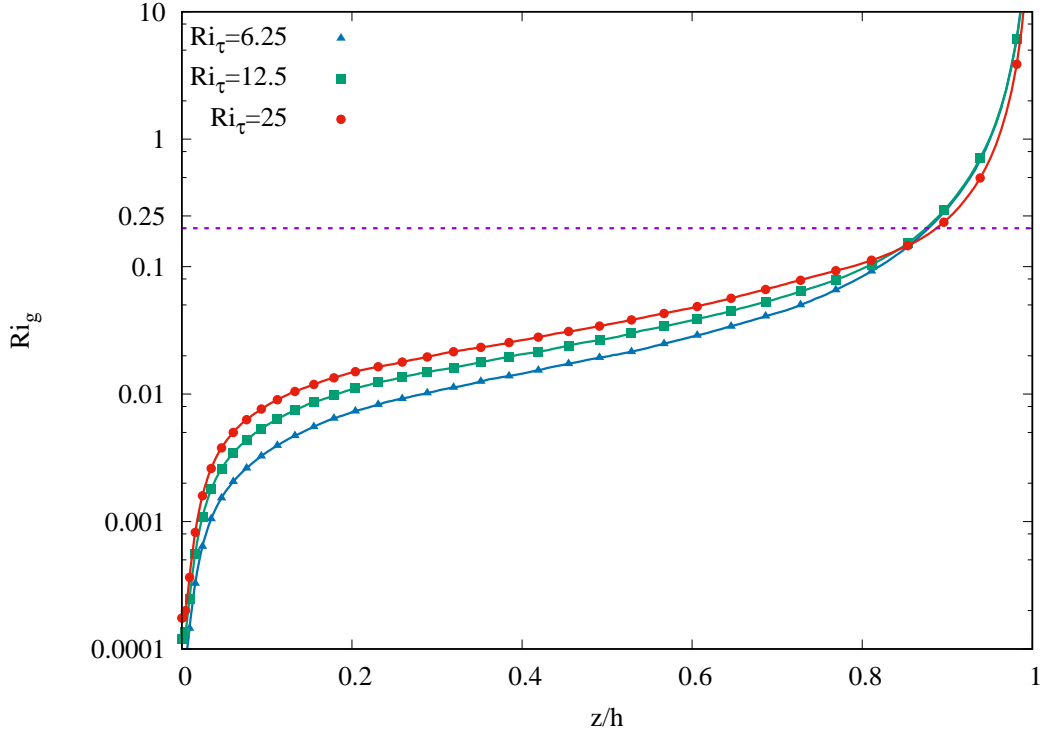
Figure 4.10: Gradient Richardson number Ri_g as a function of vertical coordinate for different Ri_τ numbers

Another important dimensionless parameter is the flux Richardson number and is defined as :

$$Ri_f = \frac{g\beta\langle T'w'\rangle}{\langle u'w'\rangle\frac{\partial\langle w\rangle}{\partial z}} \tag{4.3}$$

It represents the ratio of buoyant destruction to shear production in the turbulent kinetic energy equation[21]. In figure 4.11, the flux Richardson number is shown as a function of gradient Richardson number. The profiles collapse on the solid purple line that shows $Ri_g = Ri_f$, meaning that when Ri_g is below its critical value, the only parameter characterizing the flow is Ri_g. A similar behavior was also found by García-Villalba and Álamo [21]. For higher values of Ri_g, their data did not collapse and did not show a clear dependence on Ri_τ.
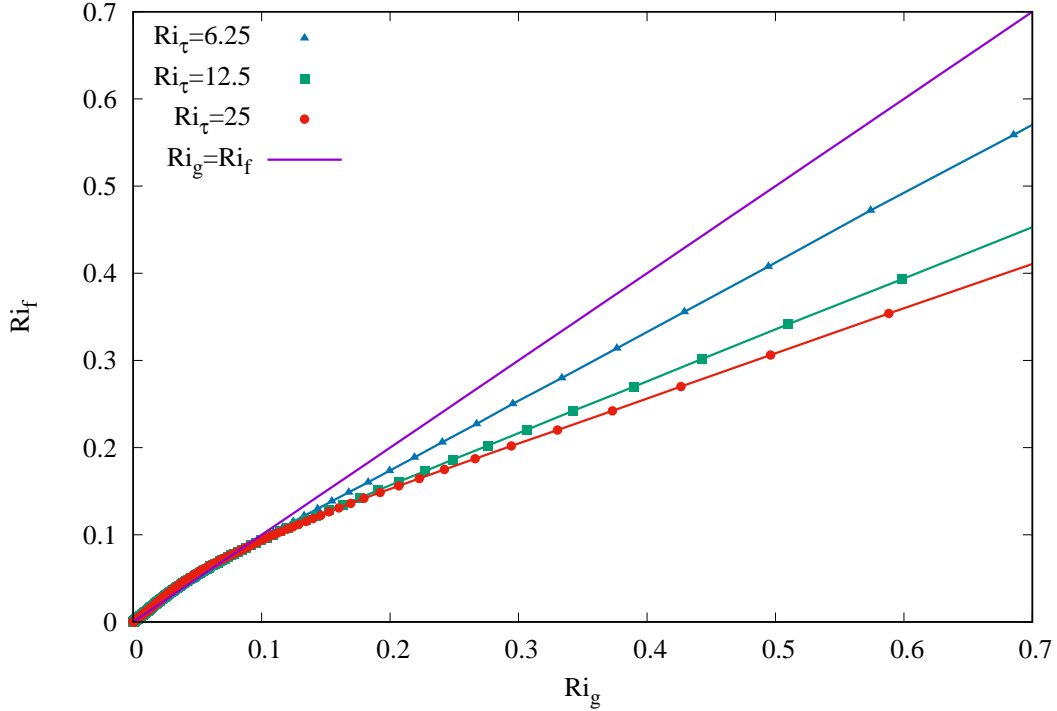
Figure 4.11: Flux Richardson number Ri_f as a function of gradient Richardson number Ri_g for different Ri_τ numbers

In the framework of turbulence modeling, a further crucial parameter is the turbulent Prandtl number Pr_T, which is defined as:

$$Pr_T = \frac{Ri_g}{Ri_f} \tag{4.4}$$

Alternatively, the turbulent Prandtl number Pr_T can also be defined as the ratio between the turbulent eddy viscosity ν_T and the turbulent eddy diffusivity κ_T (i.e. ratio between the turbulent momentum and heat fluxes). The behavior of the Pr_T as a function of the level of stratification is a challenging topic in the field of turbulence modeling [24], [69]. In figure 4.12, the turbulent Prandtl number is represented as a function of the dimensionless wall-normal coordinate. For $z^- < 0.6$, the turbulent prandtl number varies only slightly. Our results for Pr_T are in good agreement with the results of García-Villalba and Álamo [21]. The sharper variation of Pr_T for $z^- > 0.6$ is still a matter of debate, in the sense that the dependence of Pr_T on Ri_τ is not compleatly understood. This is also pointed out by García-Villalba and Álamo [21].
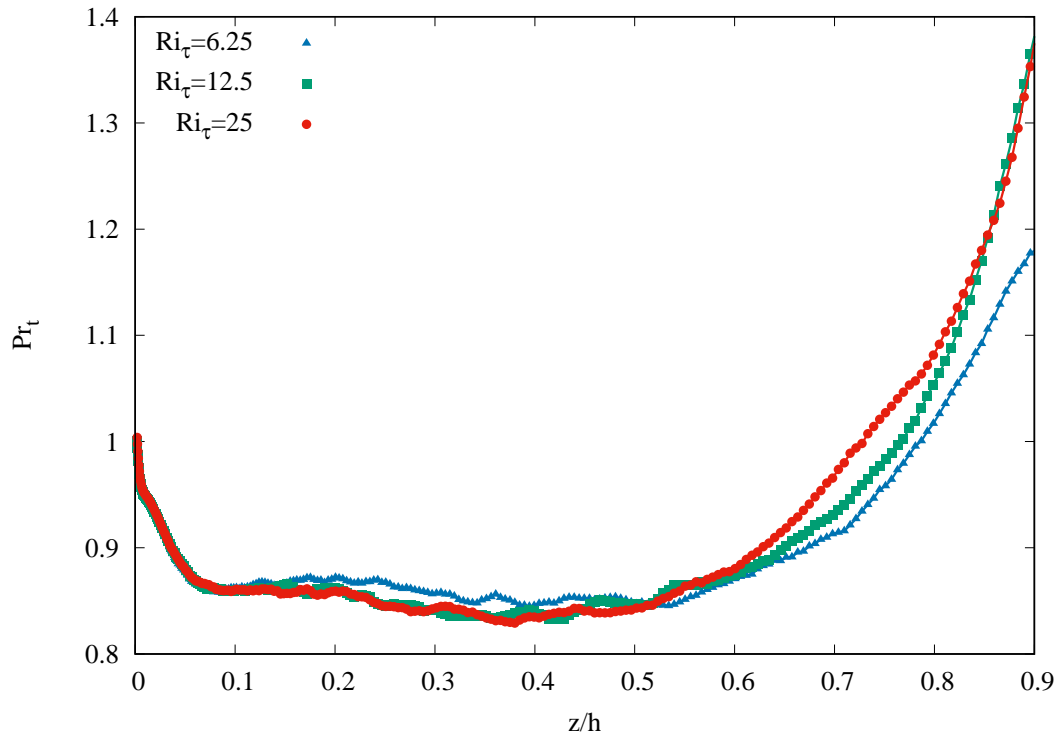
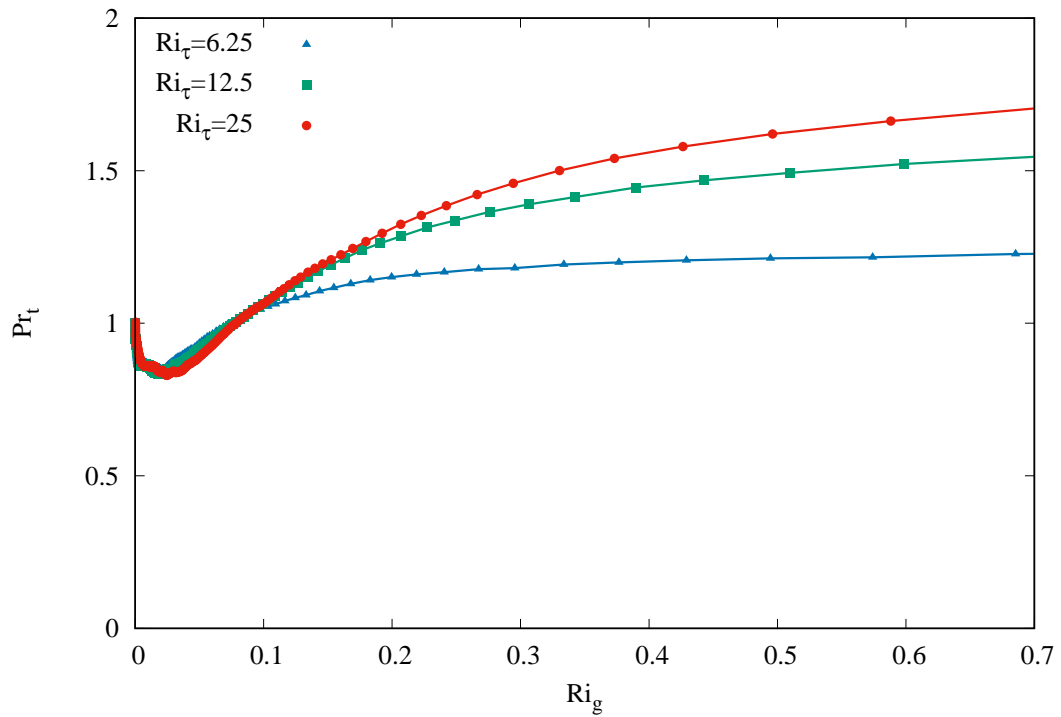Figure 4.12: Turbulent Prandtl number Pr_t as a function of vertical coordinate for different Ri_τ numbers

Figure 4.13: Turbulent Prandtl number Pr_t as a function of gradient Richardson number Ri_g for different Ri_τ numbers

In figure 4.13 the turbulent Prandtl number is represented as a function of gradient Richardson number for different shear Richardson numbers. It seems that the assumption of $Pr_T \approx 1$, customarily done in turbulence modeling, is reasonable for $Ri_g \leq 0.25$ only. Our results agree fairly well with those of García-Villalba and Álamo [21].

4.3 Qualitative behavior of the flow field

In this section, the qualitative behavior of the flow field through instantaneous visualization of the velocity and temperature field is presented in different sections of the channel. Note that, according to the spatial directions, shown in figure 3.3, a $x - z$ plane is a streamwise section, a $y - z$ plane is a cross section and a $x - y$ plane is a horizontal plane normal to the wall.

Figures 4.14-4.17 illustrate the instantaneous temperature field in a streamwise section at the center of the channel for simulations $S0$, $S1$, $S2$ and $S3$ respectively. For simulation $S0$ we observed the chaotic mixing which was expected for a neutrally-buoyant case. With increasing the level of stratification, the turbulent structure is damped through the buoyancy effects at the core region of the channel and finally in figure 4.17 for the simulation $S3$ we detected clearly the internal waves at the center of the channel. These results are consistent with what we observed in sections 4.1.1 and 4.1.2. Internal waves are found only in a narrow region of the channel near the centerline. Figures 4.18-4.21 show the instantaneous streamwise velocity on the same section and for the same Richardson numbers of those for temperature. Here again, we observed a stronger turbulent structure for simulation $S0$ at the core region of the channel as it is presented in figure 4.18, while for the simulation $S3$, figure 4.21 shows a weaker turbulent structure at the center of the channel. Increasing the extension of the dark red region at the center of the channel from figure 4.18 to 4.21 indicated a flow acceleration with increasing the level of the stratification, as already described in figure 4.1. Figures 4.22 and 4.23 illustrate the instantaneous temperature field on a spanwise section at center of the channel for two $S0$ and $S3$ simulations. The effect of buoyancy at the core region of the channel can be clearly observed from figure 4.25. In this region the chaotic mixing due to turbulence is damped because of the presence of the stratification compared to the neutrally-buoyant case. Figures 4.24 and 4.25 show the streamwise velocity on a spanwise section in the center of the channel. Figure 4.25 shows that turbulence structures in the near-wall region are still visible at $Ri_\tau = 25$. This means the stratification does not alter the near-wall region (as also observed in section 4.1.1. The only observable effect of stratification on the near-wall structures is the reduction of their extension in the wall-normal direction. For a more detailed visualization of the flow structure in the near-wall region, we plotted the streamwise velocity fluctuations in a horizontal plane parallel and near to wall at $z^+ \sim 10$ in figures 4.26 and 4.27.
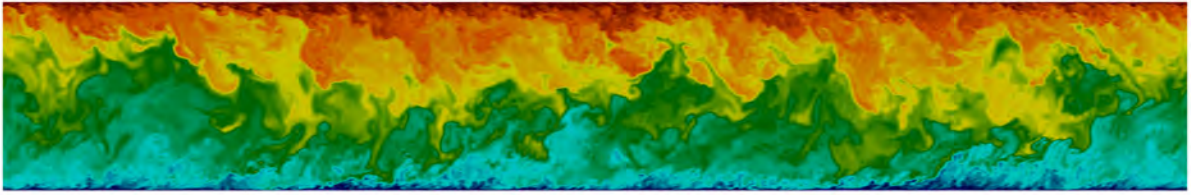
Figure 4.14: instantaneous temperature field in a streamwise section at center of the channel for $Ri_\tau = 0$
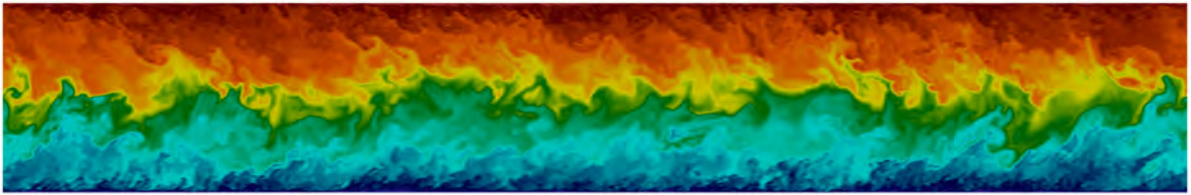

Figure 4.15: instantaneous temperature field in a streamwise section at center of the channel for $Ri_\tau = 6.25$
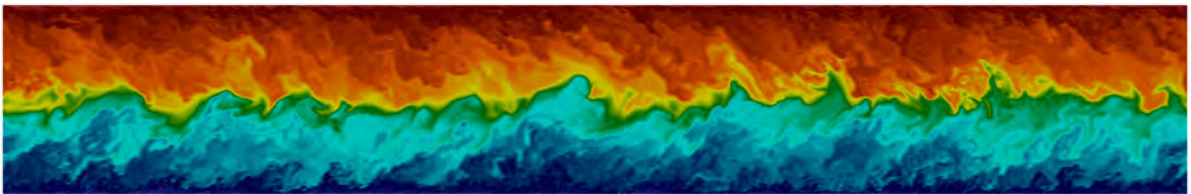

Figure 4.16: instantaneous temperature field in a streamwise section at center of the channel for $Ri_\tau = 12.5$
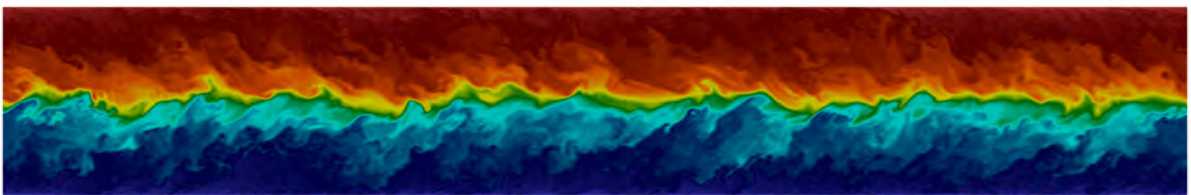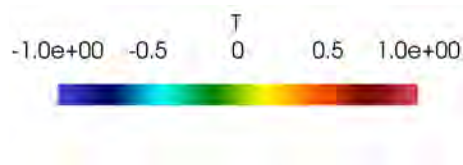

Figure 4.17: instantaneous temperature field in a streamwise section at center of the channel for $Ri_\tau = 25$
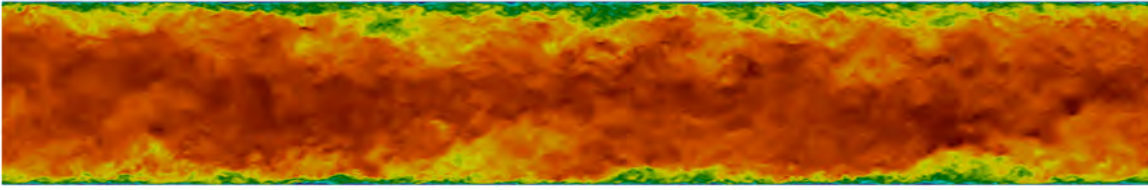
Figure 4.18: instantaneous streamwise velocity field in a streamwise section at center of the channel for $Ri_\tau = 0$
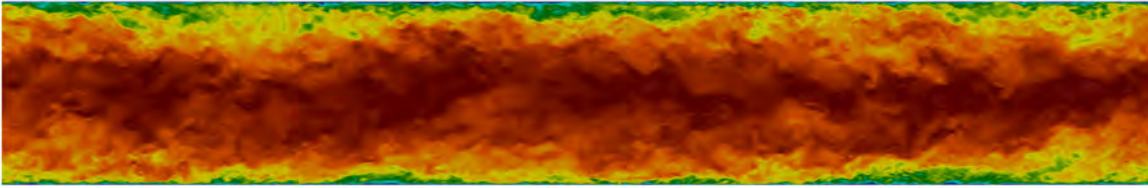

Figure 4.19: instantaneous streamwise velocity field in a streamwise section at center of the channel for $Ri_\tau = 6.25$
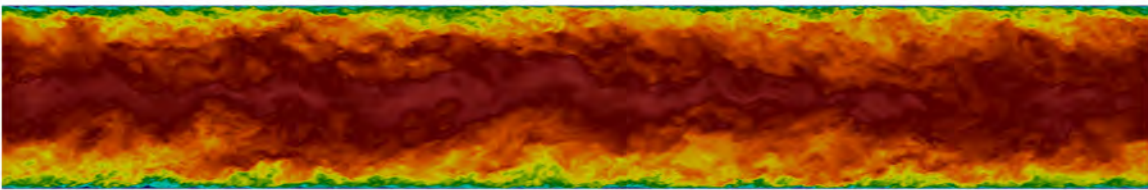

Figure 4.20: instantaneous streamwise velocity field in a streamwise section at center of the channel for $Ri_\tau = 12.5$
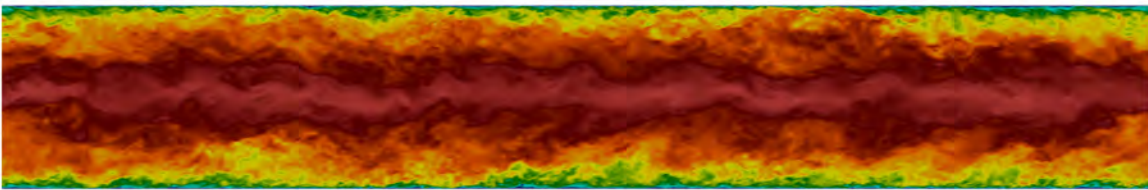

Figure 4.21: instantaneous streamwise velocity field in a streamwise section at center of the channel for $Ri_\tau = 25$
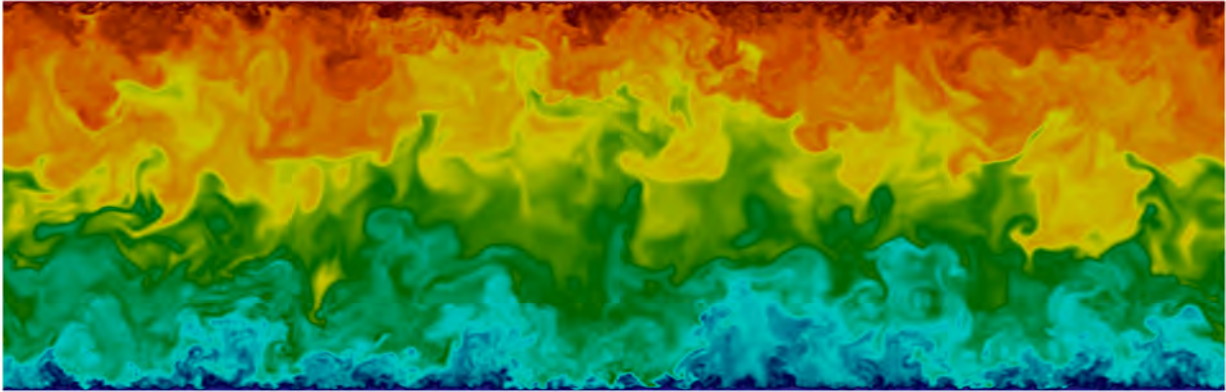
Figure 4.22: instantaneous temperature field in a spanwise section at center of the channel for $Ri_\tau = 0$
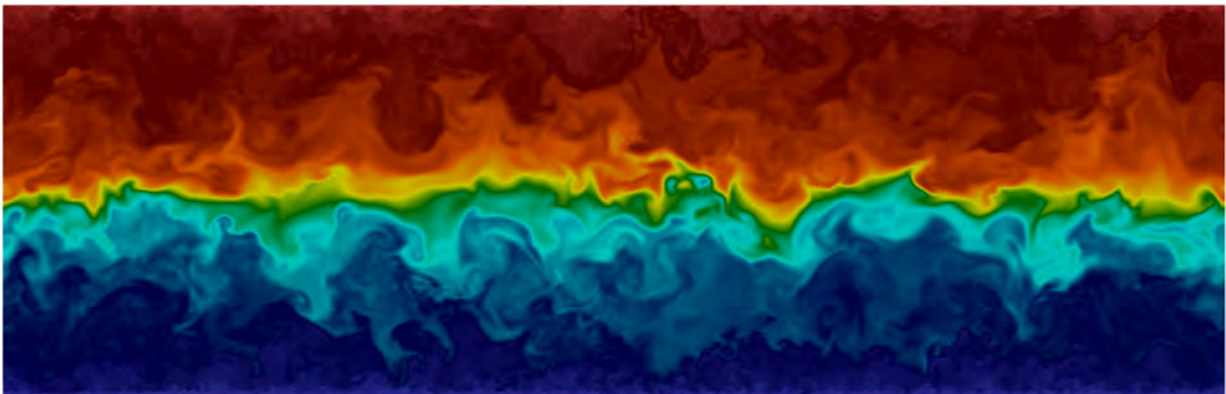
Figure 4.23: instantaneous temperature field in a spanwise section at center of the channel for $Ri_\tau = 25$

Figures 4.26 and 4.27 show a very similar structure. The similarity of streaks represent that turbulence remains active in the near-wall region even increasing the level of stratification, which was also clearly shown in Figures 4.1 and 4.2. In such a case, our results show a good agreement with García-Villalba and Álamo [21].

Figure 4.24: instantaneous streamwise velocity field in a spanwise section at center of the channel for $Ri_\tau = 0$
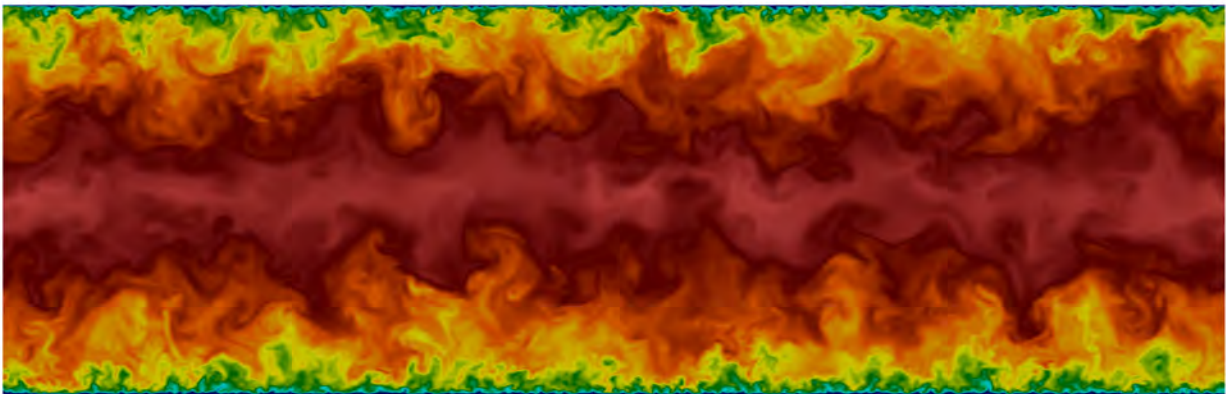
Figure 4.25: instantaneous streamwise velocity field in a spanwise section at center of the channel for $Ri_\tau = 25$
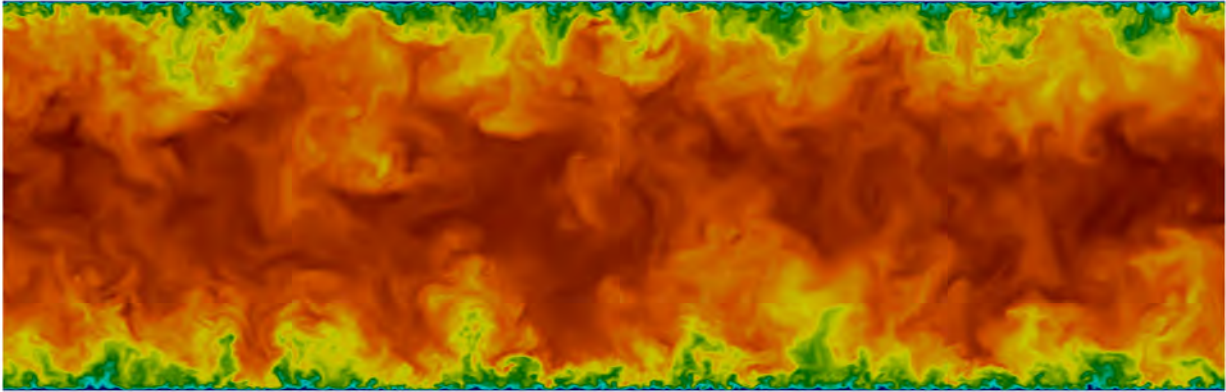
Figures 4.28 and 4.29 illustrate the temperature and wall-normal velocity fluctuations in a horizontal plane parallel to the wall at the center of the channel. The black boxes are set at the same position of the plane for both fluctuations fields.

4 Results

Figure 4.26: instantaneous streamwise velocity fluctuations in a horizontal plane parallel to the wall at $z^+ \sim 10$ for $Ri_\tau = 0$

Figure 4.27: instantaneous streamwise velocity fluctuations in a horizontal plane parallel to the wall at $z^+ \sim 10$ for $Ri_\tau = 25$
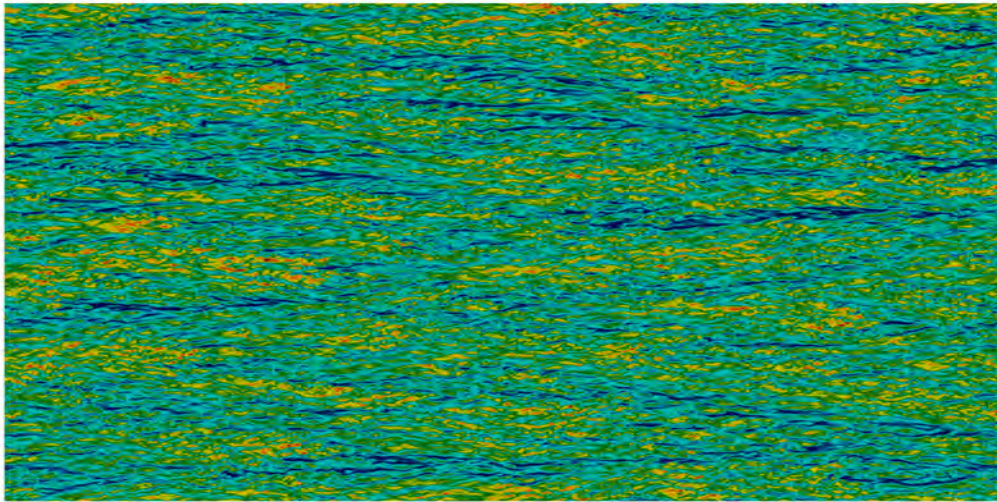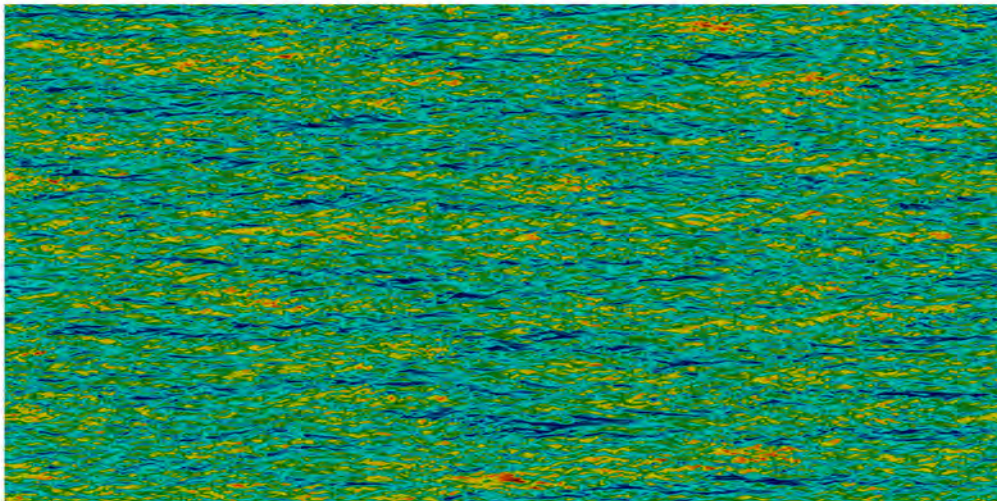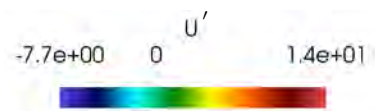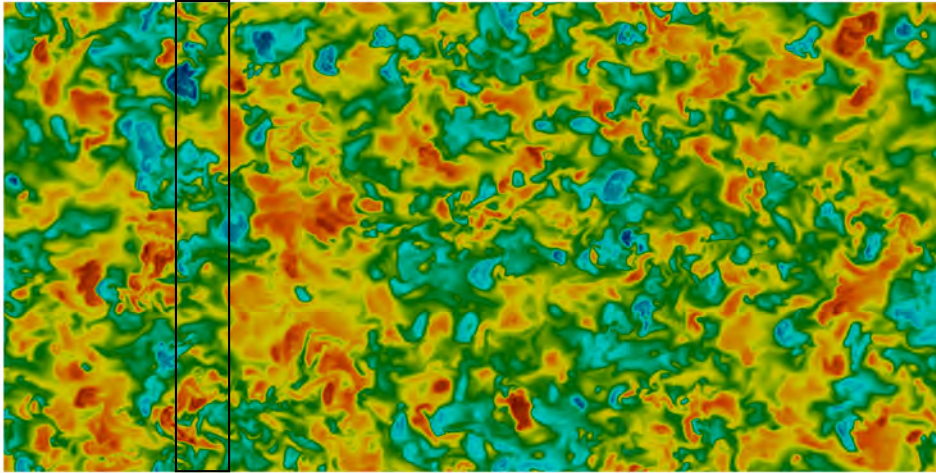
Figure 4.28: instantaneous temperature fluctuations in a horizontal plane parallel to the wall at center of the channel for $Ri_\tau = 25$
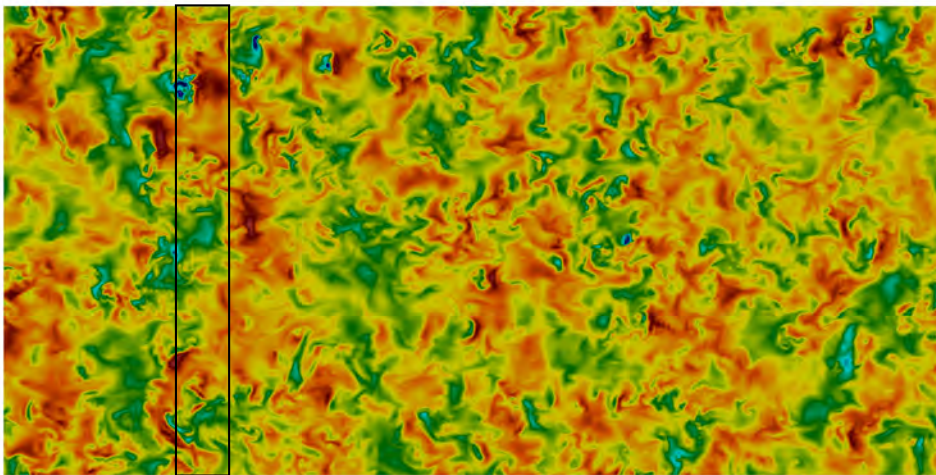
Figure 4.29: instantaneous wall-normal velocity fluctuations in a horizontal plane parallel to the wall at center of the channel for $Ri_\tau = 25$
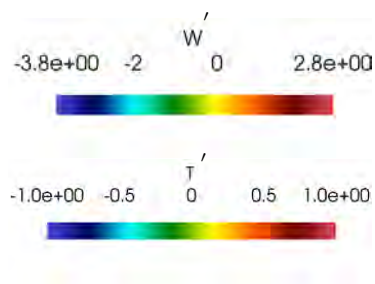
In figure 4.28, Inside the region delimited by the box, we observe a range of approximately low values of temperature fluctuations. In the same region for the wall-normal velocity fluctuations (figure 4.29), we observe a relatively higher range of value for this quantity. This is also what we observed in section 4.1.3 from figures 4.4, 4.6 and 4.7. Figures 4.28 and 4.29 quantify that the large magnitude of temperature and wall-normal velocity fluctuations can be due to the effect of buoyancy and IGW at the center of the channel, while the the correlation between these two fluctuations remains small. A phase lag of $\pi/2$ between wall-normal and temperature fluctuations is also reported by García-Villalba and Álamo [21] and Iida *et* al. [29].

5 Conclusions and Future Work

In this thesis we focused on the effect of an imposed stable stratification on the dynamics of a turbulent channel flow at high Reynolds number. To study this effect we performed numerical experiments based on a extensive campaign of direct simulations of heat and momentum transfer in turbulent channel flow under the OB approximation. Simulations were run at Reynolds number $Re_\tau = 1000$ and for different Richardson numbers. Comparison is made for the case of constant temperature boundary conditions. The temperatures at the hot wall, T_H, and at the cold wall, T_C, were varied to generate temperature differences between walls (ΔT) while maintaining a constant average reference temperature (T_0). When compared to the neutrally-buoyant case ($Ri_\tau = 0$), the statistical moments for the fluid velocity obtained for stably stratified flows exhibit significant differences throughout the entire channel, particularly in the core region of the channel. Specifically, we find that turbulence is substantially affected by buoyancy in the core region of the channel while the near-wall region retains its representative features. Near-wall turbulence for the stratified cases is similar to neutrally-buoyant wall turbulence because shear still dominates over buoyancy near the wall. Buoyancy effects dominate the central region of the channel as the mean shear vanishes due to symmetry. Flow visualizations show that internal gravity waves develop in this zone. With increasing the level of stratification, turbulent buoyancy flux become negligible in this region and, as a consequence, the mean velocity and temperature profiles show a sort of more non-turbulent behavior. This zone acts as a barrier to the momentum and buoyancy exchange , splitting the channel into two separate regions that could only through potential modes.

In terms of future works, some proposals could be recommended such as investigating the flow field under the Non-Oberbeck-Boussinesq condition, arising when large temperature gradients are present or when the typical size of the involved flow scales are large. Further attention is required by physical situations in which the fluid density depends on two scalar fields (double diffusive convection). These complex situations are ordinary occurrences in oceans, where temperature gradient is the stabilizing factor and salinity gradient produces instabilities. Different rates of temperature and salt diffusivity makes the fluid dynamics particularly rich and hard to capture [49], [72]. Finally, the stratified rotating Ekman layer could be investigated, which is crucially important for geophysical and environmental applications. In such flow instance, buoyancy effects interact with rotational effects to produce complex and hard to predict physics [2], [12], [65].

Bibliography

[1] B. Agostini, M. Fabbri, J. E. Park, L. Wojtan, J. R. Thome, and B. Michel, "State of the art of high heat flux cooling technologies", *Heat Transfer Eng.*, vol. 28, pp. 258–281, 2007.

[2] C. Ansorge and J. P. Mellado, "Global intermittency and collapsing turbulence in the stratified planetary boundary layer", *Bound.-Layer Meteor.*, vol. 153, pp. 89–116, 2014.

[3] V. Armenio and S. Sarkar, "An investigation of stably stratified turbulent channel flow using large-eddy simulation", *J. Fluid Mech.*, vol. 459, p. 1, 2002.

[4] J. H. Bae, J. Y. Yoo, and C. H., "Direct numerical simulation of turbulent super-critical flows with heat transfer", *Phys. Fluids*, vol. 17, p. 105 104, 2005.

[5] P. R. Bannon, "On the anelastic approximation for a compressible atmosphere", *J. Atmos. Sci.*, vol. 53, pp. 3618–3628, 1996.

[6] G. Batchelor, *An introduction to fluid dynamics*. Cambridge University Press, 1967.

[7] A. Bejan, *Convection heat transfer*. Wiley, 1984.

[8] J. Boussinesq, *Theorie analytique de la chaleur*. Gauthier-Villars, 1903.

[9] G. Brethouwer, Y. Duguet, and P. Schlatter, "Turbulent-laminar coexistence in wall flows with coriolis, buoyancy or lorentz forces", *J. Fluid Mech.*, vol. 704, pp. 137–172, 2012.

[10] G. N. Coleman, J. H. Ferziger, and P. R. Spalart, "Direct numerical simulation of the stably stratified turbulent ekman layer", *J. Fluid Mech.*, vol. 244, pp. 677–712, 1992.

[11] A. Cortesi, G. Yadigaroglu, and S. Banerjee, "Numerical investigation of the formation of three-dimensional structures in stably-stratified mixing layers", *Phys. Fluids*, vol. 10, pp. 1449–1473, 1998.

[12] E. Deusebio, G. Brethouwer, P. Schlatter, and E. Lindborg, "A numerical study of the unstratified and stratified ekman layer", *J. Fluid Mech.*, vol. 755, pp. 672–704, 2014.

[13] E. Deusebio, C. P. Caulfield, and J. R. Taylor, "The intermittency boundary in stratified plane couette flow", *J. Fluid Mech.*, vol. 781, pp. 298–329, 2015.

[14] E. Deusebio, P. Schlatter, G. Brethouwer, and E. Lindborg, "Direct numerical simulations of stratified open channel flows", *J. Phys. Conf. Ser.*, pp. 241–259, 2011.

[15] V. Dostal, P. Hejzlar, and M. Driscoll, "The supercritical carbon dioxide power cycle: Comparison to other advanced power cycles", *Nucl. Technol.*, vol. 154, pp. 283–301, 2006.

[16] H. J. S. Fernando, "Turbulent mixing in stratified fluids", *Annu. Rev. Fluid Mech.*, vol. 23, pp. 455–493, 1991.

[17] O. Flores and J. J. Riley, "Analysis of turbulence collapse in the stably stratified surface layer using direct numerical simulation", *Bound.-Layer Meteor.*, vol. 139, pp. 241–159, 2 2011.

[18] B. Fornberg, *A practical guide to pseudospectral methods*. Cambridge University Press, 1996.

[19] L. Fox and I. B. Parker, *Chebyshev polynomials in numerical analysis*. Oxford University Press, 1968.

[20] C. Galizzi and D. Escudié, "Experimental analysis of an oblique turbulent flame front propagating in a stratified flow", *Combust. Flame*, vol. 157, pp. 2277–2285, 2010.

[21] M. García-Villalba and J. C. D. Álamo, "Turbulence modification by stable stratification in channel flow", *Phys. Fluids*, vol. 23(4), p. 045 104, 2011.

[22] R. P. Garg, J. H. Ferziger, S. G. Monismith, and J. R. Koseff, "Stably stratified turbulent channel flows. i. stratification regimes and turbulence suppression mechanism", *Phys. Fluids*, vol. 12, 2000.

[23] B. Gebhart, Y. Jaluria, R. L. Mahajan, and B. Sammakia, *Buoyancy-induced flows and transport*. Hemisphere Publishing Corporation, 1988.

[24] A. A. Grachev, E. L. Andreas, C. W. Fairall, P. S. Guest, and P. O. G. Persson, "On the turbulent prandtl number in the stable atmospheric boundary layer", *Boundary-Layer Meteorology*, vol. 125(2), pp. 329–341, 2007.

[25] D. Gray and A. Giorgini, "The validity of the boussinesq approximation for liquids and gases", *Int. J. Heat Mass Transfer*, vol. 19, pp. 545–551, 1976.

[26] P. He, "A high order finite difference solver for massively parallel simulations of stably stratified turbulent channel flows", *Comput. Fluids*, vol. 127, pp. 161–173, 2016.

[27] S. E. Holt, J. R. Koseff, and J. H. Ferziger, "A numerical study of the evolution and structure of homogeneous stably stratified sheared turbulence", *J. Fluid Mech.*, vol. 237, pp. 499–539, 1992.

[28] ——, "A numerical study of the evolution and structure of homogeneous stably stratified sheared turbulence", *Phys. Fluids*, vol. 237, p. 499, 1992.

[29] O. Iida, N. Kasagi, and Y. Nagano, "Direct numerical simulation of turbulent channel flow under stable density stratification", *Intl. J. Heat Mass Transfer*, vol. 45, 2002.

[30] G. N. Ivey, K. B. Winters, and J. R. Koseff, "Density stratification, turbulence, but how much mixing?", *Annu. Rev. Fluid Mech.*, vol. 40, p. 169, 2008.

[31] P. K. Kundu, I. M. Cohen, and D. R. Dowling, *Fluid mechanics 5th edition*. Academic Press, 2011.

[32] D. K. Lilly, "Stratified turbulence and the mesoscale variability of the atmosphere", *J. Atmos. Sci.*, vol. 40, pp. 749–761, 1983.

[33] ——, "A comparison of incompressible, anelastic and boussinesq dynamics", *Atmos. Res.*, vol. 40, pp. 143–151, 1996.

[34] E. Lindborg, "The energy cascade in a strongly stratified fluid", *J. Fluid Mech.*, vol. 550, pp. 207–242, 2006.

[35] S. Lovecchio, F. Zonta, and A. Soldati, "Influence of thermal stratification on the surfacing and clustering of floaters in free surface turbulence", *Adv. Water Resour.*, vol. 72, pp. 22–31, 2014.

[36] L. Mahrt, "Stratified atmospheric boundary layers", *Bound.-Layer Meteor.*, vol. 90, pp. 375–396, 1999.

[37] ——, "Stably stratified atmospheric boundary layers", *Annu. Rev. Fluid Mech.*, vol. 46, pp. 23–45, 2014.

[38] J. M. Mihaljan, "A rigorous exposition of the boussinesq approximations applicable to a thin layer of fluid", *Astrophys J.*, vol. 136, pp. 1126–1133, 1962.

[39] J. W. Miles, "On the stability of heterogeneous shear flows", *J. Fluid Mech.*, vol. 10(4), pp. 496–508, 1961.

[40] A. S. Monin and A. M. Obukhov, "Basic laws of turbulent mixing in the surface layer of the atmosphere", *Contrib. Geophys. Inst. Acad. Sci. USSR*, vol. 151, no. 163–187, 1954.

[41] A. S. Monin and A. M. Yaglom, *Statistical fluid mechanics: Mechanism of turbulence, book 2*. MIT Press, 1975.

[42] H. Nemati, P. A., B. J. Boersma, and P. R., "Mean statistics of a heated turbulent pipe flow at supercritical pressure", *Intl. J. Heat Mass Transfer*, vol. 83, pp. 741–752, 2015.

[43] J. J. Niemela, "High rayleigh number thermal convection", *J. Low Temp. Phys.*, vol. 134, pp. 447–456, 2004.

[44] J. J. Niemela and K. Sreenivasan, "The use of cryogenic helium for classical turbulence: Promises and hurdles", *J. Low Temp. Phys.*, vol. 143, pp. 163–212, 2006.

[45] F. T. M. Nieuwstadt, "Direct numerical simulation of stable channel flow at large stability", *Bound.-Layer Meteor.*, vol. 116, pp. 277–299, 2005.

[46]   A. Oberbeck, "Über die wärmeleitung der flüssigkeiten bei berücksichtigung der strö-mungen infolge von temperaturdifferenzen", *Ann. Phys. Chem.*, vol. 243, pp. 271–292, 1879.

[47]   A. M. Obukhov, "Turbulence in the atmosphere with a non-uniform temperature", *Bound.-Layer Meteor.*, vol. 2, no. 7–29, 1971.

[48]   Y. Ogura and N. Phillips, "Scale analysis of deep and shallow convection in the atmosphere", *J. Atmos. Sci.*, vol. 19, pp. 173–179, 1962.

[49]   F. Paparella and J. V. Hardenberg, "Clustering of salt fingers in double-diffusive convection leads to staircaselike stratification", *Phys. Rev. Lett.*, vol. 109, p. 014 502, 2012.

[50]   P. Piccirillo and C. W. Van Atta, "The evolution of a uniformly sheared thermally stratified turbulent flow", *J. Fluid Mech.*, vol. 334, pp. 61–86, 1997.

[51]   G. L. Pickard and W. J. Emery, *Descriptive physical oceanography: An introduction.* Pergamon Press, 1990.

[52]   S. S. Pitla, D. M. Robinson, E. A. Groll, and S. Ramadhyani, "Heat transfer from supercritical carbon dioxide in tube flow: A critical review", *Hvac&R Res.*, vol. 4, pp. 281–301, 2006.

[53]   M. Pons and P. Le Quéré, "Modeling natural convection with the work of pressure-forces: A thermodynamic necessity", *Int. J. Numer. Meth. Fluids*, vol. 13, pp. 322–332, 2007.

[54]   S. B. Pope, *Turbulent flows.* Cambridge University Press, 2000.

[55]   J. J. Riley and M.-P. Lelong, "Fluid motion in the presence of strong stable stratification", *Annu. Rev. Fluid Mech.*, vol. 32, pp. 613–657, 2000.

[56]   J. J. Rohr, E. C. Itsweire, K. N. Helland, and C. N. Van Atta, "Numerical simulations of the freely evolving turbulence in stably stratified fluids", *J. Fluid Mech.*, vol. 195, p. 77, 1988.

[57]   J. J. Rohr, E. C. Itsweire, K. N. Helland, and C. W. Van Atta, "Growth and decay of turbulence in a stably stratified shear flow", *J. Fluid Mech.*, vol. 195, pp. 77–111, 1988.

[58]   J. J. Rohr, E. C. Itsweire, K. N. Helland, and C. W. van Atta, "Growth and decay of turbulence in a stratified shear flows", *J. Fluid Mech.*, vol. 195, pp. 77–111, 1988.

[59]   A. Sameen, V. R., and S. K. R., "Specific role of fluid properties in non-boussinesq thermal convection at the rayleigh number of 2×10^8", *Europhys. Lett.*, vol. 86, p. 14 006, 2009.

[60]   W. D. Smyth and J. N. Moum, "Anisotropy of turbulence in stably stratified mixing layers", *Phys. Fluids*, vol. 12, pp. 1343–1362, 2000.

[61]   ——, "Length scales of turbulence in stably stratified mixing layers", *Phys. Fluids*, vol. 12, pp. 1327–1342, 2000.

[62] E. A. Spiegel and V. G., "On the boussinesq approximation for a compressible fluid", *Astrophys J.*, vol. 131, pp. 442–447, 1960.

[63] C. Staquet and J. Sommeria, "Internal gravity waves: From instabilities to turbulence", *Annu. Rev. Fluid Mech.*, vol. 34, pp. 559–593, 2002.

[64] K. Sugiyama, E. Calzavarini, S. Grossmann, and D. Lohse, "Flow organization in two-dimensional non-oberbeck-boussinesq rayleigh-benard convection in water", *J. Fluid Mech.*, vol. 637, pp. 105–135, 2009.

[65] J. R. Taylor and S. Sarkar, "Direct and large eddy simulations of a bottom ekman layer under an external stratification", *Intl. J. Heat and Fluid Flow*, vol. 29, pp. 721–732, 2008.

[66] J. R. Taylor, S. Sarkar, and V. Armenio, "Large eddy simulation of stably stratified open channel flow", *Phys. Fluids*, vol. 95, p. 116 602, 2005.

[67] D. J. Tritton, *Physical fluid dynamics*. Oxford University Press, 1988.

[68] J. S. Turner, *Buoyancy effects in fluids*. Cambrodge University Press, 1973.

[69] S. K. Venayagamoorthy and D. D. Stretch, "On the turbulent prandtl number in homogeneous stably stratified turbulence", *J. Fluid Mech.*, vol. 644, pp. 359–369, 2010.

[70] N. Williamson, S. W. Armfield, M. P. Kirkpatrick, and S. E. Norris, "Transition to stably stratified states in open channel flow with radiative surface heating", *J. Fluid Mech.*, vol. 766, pp. 528–555, 2015.

[71] C. Wunsch and R. Ferrari, "Vertical mixing, energy, and the general circulation of the oceans", *Annu. Rev. Fluid Mech.*, vol. 36, pp. 281–314, 2004.

[72] Y. Yang, R. Verzicco, and D. Lohse, "Scaling laws and flow structures of double diffusive convection in the finger regime", *J. Fluid Mech.*, vol. 802, pp. 667–689, 2016.

[73] K. Yeo, B. G. Kim, and C. Lee, "Eulerian and lagrangian statistics in stably stratified turbulent channel flows", *J. Turbul.*, vol. 10, pp. 1–26, 2009.

[74] F. Zonta, C. Marchioli, and A. Soldati, "Modulation of turbulence in forced convection by temperature-dependent viscosity", *J. Fluid Mech.*, vol. 697, pp. 150–174, 2012.

[75] F. Zonta, M. Onorato, and A. Soldati, "Turbulence and internal waves in stably-stratified channel flow with temperature-dependent fluid properties", *J. Fluid Mech.*, vol. 697, p. 175, 2012.

[76] F. Zonta and A. Soldati, "Effect of temperature-dependent fluid properties on heat transfer in turbulent mixed convection", *J. Heat Transfer - Trans. ASME*, vol. 136, p. 022 501, 2014.

[77] ——, "Stably stratified wall-bounded turbulence", *ASME. Appl. Mech. Rev.*, vol. 70(4), 2018.